1 **Observationally constrained analysis of sulfur cycle in the marine atmosphere with NASA**
2 **ATom measurements and AeroCom model simulations**

4 Huisheng Bian[1,2], Mian Chin[2], Peter R. Colarco[2], Eric C. Apel[3], Donald R. Blake[4], Karl Froyd[5], Rebecca S.
5 Hornbrook[3], Jose Jimenez[5,6], Pedro Campuzano Jost[5,6], Michael Lawler[5,7], Mingxu Liu[8], Marianne Tronstad Lund[9],
6 Hitoshi Matsui[8], Benjamin A. Nault[5,6,10,11], Joyce E. Penner[12], Andrew W. Rollins[5,13], Gregory Schill[7], Ragnhild B.
7 Skeie[9], Hailong Wang[14], Lu Xu[15,16], Kai Zhang[14], and Jialei Zhu[17]
8
9 [1]Goddard Earth Sciences Technology and Research (GESTAR) II, University of Maryland at Baltimore County,
10 Baltimore, MD, USA.
11 [2]NASA Goddard Space Flight Center, Greenbelt, MD, USA.
12 [3]Atmospheric Chemistry Observations & Modeling Laboratory, National Center for Atmospheric Research,
13 Boulder, CO, USA.
14 [4]Department of Chemistry, University of California Irvine, CA, USA.
15 [5]Cooperative Institute for Research in Environmental Sciences, University of Colorado, Boulder, CO, USA.
16 [6]Department of Chemistry, University of Colorado, Boulder, CO, USA.
17 [7]NOAA Chemical Sciences Laboratory, Boulder, CO, USA.
18 [8]Graduate School of Environmental Studies, Nagoya University, Nagoya, Japan.
19 [9]CICERO Center for International Climate Research, Oslo, Norway.
20 [10]Now at: Department of Environmental Health and Engineering, Whiting School of Engineering, The Johns
21 Hopkins, Baltimore, MD, USA.
22 [11]Now at: Center for Aerosol and Cloud Chemistry, Aerodyne Research, Inc., Billerica, MA, USA
23 [12]Dept. of Atmospheric, Oceanic and Space Sciences, University of Michigan, Ann Arbor, Michigan, USA.
24 [13]NOAA Earth System Research Laboratory, Chemical Sciences Division, Boulder, CO, USA.
25 [14]Atmospheric Sciences and Global Change Division, Pacific Northwest National Laboratory, Richland, WA, USA.
26 [15]Division of Geological and Planetary Sciences, California Institute of Technology, Pasadena, CA, USA.
27 [16]Now at Department of Energy, Environmental and Chemical Engineering, Washington University in St. Louis,
28 Missouri, USA.
29 [17]Institute of Surface-Earth System Science, School of Earth System Science, Tianjin University, Tianjin, China.
30
31 *Correspondence to*: Huisheng Bian (huisheng.bian@nasa.gov)

33 **Abstract**

34 The atmospheric sulfur cycle plays a key role in air quality, climate, and ecosystems, such as
35 pollution, radiative forcing, new particle formation, and acid rain. In this study, we compare the
36 spatially and temporally resolved measurements from the NASA ATom mission with
37 simulations from five AeroCom-III models for four sulfur species (dimethyl sulfide (DMS),
38 sulfur dioxide (SO_2), particulate methanesulfonate (MSA), and particulate sulfate (SO_4)). We
39 focus on remote regions over the Pacific, Atlantic, and Southern Oceans from near the surface to
40 ~12-km altitude range covering all four seasons. In general, the differences among model results
41 can be greater than one-order of magnitude. Comparing with observations, model-simulated SO_2
42 is generally low wheras SO_4 is generally high. Simulated DMS concentrations near the sea
43 surface exceed observed levels by a factor of five in most cases, suggesting potential
44 overestimation of DMS emissions in all models. With GEOS model simulations of tagging
45 emission from anthropogenic, biomass burning, volcanic, and oceanic sources, we find that
46 anthropogenic emissions are the dominant source of sulfate aerosol (40-60% of the total amount)
47 in the ATom measurements at almost all altitudes, followed by volcanic emissions (18-32%) and
48 oceanic sources (16-32%). Similar source contributions can also be derived at broad ocean basins
49 and on monthly scales, indicating the representativeness of ATom measurements for global
50 ocean. Our work presents the first assessment of AeroCom sulfur study using ATom

51 measurements, providing directions for improving sulfate simulations, which remain the largest
52 uncertainty in radiative forcing estimates in aerosol climate models.
53
54 **1. Introduction**
55 Atmospheric sulfur species have wide-ranging environmental and health impacts. About two-
56 third of sulfur emissions come from anthropogenic activities (Chin et al., 2000); therefore,
57 considerable efforts have been made to reduce these sulfur emissions. For example, acid rain
58 occurs when sulfur dioxide (SO_2) is oxidized to form sulfuric acid and particulate sulfate (SO_4),
59 which fall to the ground with the rain (Bian et al., 1993; Grennfelt et al., 2020) and can devastate
60 aquatic ecosystems (Josephson et al., 2014; McDonnell et al., 2021). Through the competing
61 neutralization reaction of SO_4 and nitrate with NH_3 and other alkaline species, SO_4 affects
62 strongly both particulate nitrate formation (Bian et al., 2017) and aerosol pH (Huang et al., 2020;
63 Nault et al., 2021). Sulfate is a key component of particulate matter (PM), which degrades air
64 quality (Dong et al., 2018; Tan et al., 2018) and directly reflects the solar radiation (Moch et al.,
65 2022; Myhre et al., 2013). Due to its highly hygroscopic nature, sulfate aerosols act as effcient
66 cloud condensatin nucleus (Boucher et al., 2013; Breen et al., 2021; Seinfeld et al., 2016) and
67 thus indirectly radiative forcing (Penner et al., 2016; Wang et al., 2021) through aerosol-cloud
68 interactions. The contribution of aerosols to atmospheric clouds and energy budget remains the
69 largest uncertainty in climate models (Gryspeerdt et al., 2023; Jia et al., 2021, 2022; Klein et al.,
70 2013; Malavelle et al., 2017). Sulfate is important primarily because the atmospheric sulfate
71 component itself contributes to radiative forcing (RF) almost as much as all other major non-
72 natural aerosol components, as concluded from 16 AeroCom model studies (Myhre et al., 2013).
73 More importantly, uncertainty in sulfate simulations in current climate models is a major
74 contributor to biases in aerosol optical depth (AOD, Fig. 3 in Gliß et al., 2021) and RF (Fig. 7 in
75 Myhre et al., 2013).
76
77 Unlike other major atmospheric aerosols, a significant fraction (i.e., roughly a quarter) of sulfate
78 in the atmosphere comes from marine biological emissions (Chin et al., 1996). The impact of
79 oceanic sulfate is particularly pronounced on marine shallow clouds, which are characterized by
80 low droplet number concentrations and weak updraft velocities (Rissman et al., 2004). Sulfur
81 research has also focused on the tropical upper troposphere (TUT), where the growth of new
82 aerosol particles and homogeneous nucleation involving sulfuric acid is at a maximum
83 (Williamson et al., 2019), and where deep convective transport allows a small portion of the
84 sources to reach the lower stratosphere. The resulting sulfate aerosols in the stratosphere can
85 persist for years (Holton et al., 1995). Unfortunately, the observations in the TUT region and
86 above are sparse. Acquiring atmospheric composition and its chemical/physical properties over
87 remote oceans is challenging, although satellites can often provide total column constraints of
88 aerosol optical depth.
89
90 The NASA Earth Venture Suborbital (EVS-2) Atmospheric Tomography (ATom) airborne
91 mission provided abundant measurements of gases and aerosols over the world's oceans (Hodzic
92 et al., 2020; Thompson et al., 2021). In particular, a suite of instruments integrated on the NASA
93 Douglas DC-8 jetliner (hereafter DC-8) made measurements of many important sulfur species
94 including dimethyl sulfide (DMS), SO_2, particulate methanesulfonate (MSA) and SO_4 over the
95 Pacific and Atlantic Oceans in both hemispheres and the Southern Ocean in all four seasons.
96 These regions provide us with highly heterogeneous natural and anthropogenic source

97   environments, which is not usually the case for traditional continental studies. The
98   comprehensive ATom sulfur dataset provides us with unprecedented opportunities to assess
99   sulfur source, transport, chemistry, deposition, and particle activation and growth represented in
100   the global aerosol models, and to estimate the extent of anthropogenic influence on remote
101   oceanic atmospheric composition and cloud properties.

102

103   This study has two specific scientific goals. First, we explore the vertical and seasonal variation
104   of sulfur species (i.e., DMS, SO_2, MSA, and SO_4) using ATom measurements and simulations
105   from five global models that participated in the AeroCom-ATom model experiments. AeroCom
106   is an international initiative of scientists aiming at the advancement of the understanding of the
107   global aerosol and its impact on climate (https://aerocom.met.no/). Here we focus on remote
108   regions over the Pacific, Atlantic, and Southern Oceans, from near the surface to an altitude of
109   about 12 km, covering all four seasons. Second, we determine whether the produced SO_4
110   originated from anthropogenic or natural sources by using tagged tracers associated with
111   emission types.

112

113   Our work is the first study to use ATom measurements for comparison with the AeroCom
114   models, focusing on all sulfur species simulated in current aerosol climate models. This work
115   extends previous efforts using ATom measurements to evaluate the organic carbon (Hodzic et
116   al., 2020) and black carbon (Katich et al., 2018) of AeroCom models, as well as individual
117   models focusing on new particle formation in the tropics (Williamson et al., 2019), fine aerosol
118   lifetime (Gao al. al., 2022), aerosol vertical transport (Yu et al., 2019), sea salt (Bian et al.,
119   2019), smoke (Schill et al., 2020), mineral dust (Froyd et al., 2022), and DMS chemistry (Fung
120   et al., 2022). Furthermore, to our knowledge, there are no studies that systematically investigate
121   the changes and sources of all major sulfur species over the remote ocean. Our study aims not
122   only to reveal sulfur variability based on multiple measurements and model simulations, but also
123   to tease out the underlying processes behind the variability through a comprehensive analysis of
124   simulated sulfur species in aerosol climate models.

125

126   The structure of this paper is as follows. Section 2 describes the ATom measurements and the
127   AeroCom models used in this study. Section 3 presents the ATom-AeroCom sulfur comparison
128   from different perspectives, namely the overall comparison in Sect. 3.1, the vertical profiles in
129   Sect. 3.2, and the regional and seasonal analysis in Sect. 3.3. The sulfur budget analysis is given
130   in Sect. 4. We further present investigations of source origins for aerosol SO_4 along flight tracks
131   and over oceans in Sect. 5. Finally, we summarize our findings in Sect. 6.

132

133   **2. Data**
134   **2.1 ATom measurements**
135   ATom was a NASA-funded Earth Venture Suborbital project designed to study the effects of air
136   pollution on chemically reactive gases, aerosols, and greenhouse gases in the remote atmosphere.
137   ATom deployed a large suite of gas and aerosol measurement instruments on the NASA DC-8
138   aircraft for systematic sampling, covering an extended region of the globe from 85°N to 85°S
139   over the Pacific and Atlantic Oceans, with vertical profiles from near-surface to near-tropopause
140   (i.e., 0.2-12 km, Thompson et al., 2021). Four ATom deployments (ATom-1 to -4) were
141   executed over each of the four seasons from 2016 to 2018, and their flight paths are shown in
142   Fig. 1. The extensive aerosol and gas measurements made during ATom include inorganic and

143 organic aerosols, precursor gases, particle size distributions and particle composition. Table 1
144 lists the instruments for ATom sulfur species observations used in this study including the
145 relevant sampling details needed for the model comparison.
146
147 We use SO_4 and MSA that had been measured by two instruments, the University of Colorado
148 Aerodyne high-resolution time-of-flight aerosol mass spectrometer (AMS, Canagaratna et al.,
149 2007; Guo et al., 2021), and the NOAA Particle Analysis by Laser Mass Spectrometry (PALMS,
150 Froyd et al., 2019). The latter makes *in situ* measurements of the chemical composition of
151 individual aerosol particles. Furthermore, AMS measured submicron aerosols while PALMS
152 provided mass mixing ratio and size distribution up to 3 µm in dry diameter (Brock et al., 2019).
153 It is worth noting that AMS data were independently processed and reported at both 1-s and 60-s
154 time resolutions by instrument PI (Jimenez et al., 2019). The detection limit varied with different
155 averaging time resolutions, and they were provided directly for each sampling point in AMS
156 datasets. Some negative measurements were also presented in AMS datasets, and this is normal
157 for measurements of very low concentrations in the presence of instrumental noise. The AMS
158 data at 60-s resolution is recommended owing to more robust peak fitting at low concentrations
159 (Hodzic et al., 2020). Given the complex data overlays (i.e., starting, ending, and frequency)
160 reported from multiple instruments, the ATom team also provide a 10-s merged dataset to
161 facilitate users' applications. In this study, we evaluate data reported in different time
162 resolutions, using AMS as an example, to ensure the quality of merged data that are exclusively
163 used as the primary dataset in this work.
164
165 Two instruments were used for SO_2 measurements: the California Institute of Technology
166 Chemical Ionization Mass Spectrometer (CIMS) and the NOAA Laser Induced Fluorescence
167 (LIF) (Table 1). The CIMS uses CF_3O^- as a reagent ion which reacts with SO_2 via fluoride ion
168 transfer chemistry. The product ion is detected by a compact time-of-flight mass spectrometer
169 (CToF). The precision of the CIMS SO_2 measurement decreases with increasing water vapor
170 concentration (Eger et al., 2019; Huey et al., 2004; Jurkat et al., 2016; Rickly et al., 2021),
171 making it challenging to measure SO_2 in remote ocean regions. In these regions, the ambient
172 water vapor may be sufficiently high that the CIMS SO_2 precision at 1-s resolution (~130 parts
173 per trillion by volume, pptv) is insufficient for measuring ambient SO_2 value there (<100 pptv).
174 To address this shortcoming, the ATom science team added a new instrument, the NOAA LIF, to
175 the ATom-4 payload. The NOAA LIF instrument uses red-shifted laser-induced fluorescence to
176 detect SO_2 at very low ppt levels (Rickly et al., 2021; Rollins et al., 2016). Both instruments
177 report negative values and the detection limit of the LIF instrument is about 2 pptv.
178
179 DMS was measured during ATom by two instruments, the University of California, Irvine
180 Whole Air Sampler (WAS), and the NCAR Trace Organic Gas Analyzer (TOGA). The WAS
181 reported DMS for all four ATom deployments, while the TOGA reported data for ATom-2 to -4
182 and not for ATom-1 due to possible issues associated with the TOGA inlet (the inlet was
183 changed for ATom-2 to -4). Both instruments have comparable detection limit (1 pptv) and
184 accuracy (~15%). However, the sampling time interval of WAS (variable but ~180s) was longer
185 than TOGA (~120s).
186
187 **2.2 AeroCom models**

188 Five global aerosol models participated in an AeroCom-ATom model experiment
189 (https://wiki.met.no/aerocom/phase3-experiments): CAM-ATRAS, E3SM, GEOS, IMPACT,
190 and OsloCTM3. The experiment required all participating models to (1) conduct three-year-
191 simulations of 2016-2018 (i.e., covering the whole ATom observation period); (2) use or nudge
192 meteorological data for the simulation period; and (3) use the same pre-defined emission fields
193 for precursor gases and aerosol tracers. The suggested emissions are the Coupled Model
194 Intercomparison Project Phase 6 Community Emissions Data System (CEDS, Hoesly et al.,
195 2018) for anthropogenic source, daily biomass burning emission (such as The Global Fire
196 Assimilation System, GFAS), a dataset based on satellite volcanic SO_2 observations from the
197 OMI instrument on the Aura satellite (Carn et al., 2016, 2017) for outgassing and eruptive
198 volcanic emission, and DMS concentration in sea surface from Lana et al. (2011). Wind-driven
199 emissions, such as dust and sea salt, are calculated online by each model. Table 2 summarizes
200 the detailed model characteristics and input datasets relevant to this study. It is worth noting that
201 CEDS specifies anthropogenic emissions from various sectors, including emissions from
202 shipping. The version of CEDS used in this work has emissions up to 2014 and all models use
203 2014 emission for ATom periods. Furthermore, unlike other models that use CEDS emissions,
204 the anthropogenic emissions of OsloCTM3 are obtained following Shared Socioeconomic
205 Pathways (SSP) under Representative Concentration Pathway (RCP) scenario with medium
206 radiative forcing by the end of the century (SSP245, Fricko et al., 2017), and the emissions are
207 interpolated to 2016 and 2017. Following the experimental protocol, all models provided results
208 for all ATom periods except for OsloCTM3 that omitted data in ATom-4. Unlike traditional
209 AeroCom experiments that used gridded daily/monthly averaged data, modelers are required to
210 interpolate model results along flight track every 10 s (see more discussion in Sect. 3.1) using
211 three-dimensional high frequency (e.g., hourly or even less depending on the models' time step)
212 data to facilitate the comparison. It is worth noting that the models do not have any actual
213 information at 10-s time resolution, given their time steps are at least 10× greater and their
214 spatial resolutions are coarse. However, the interpolation methodology suggested here provides
215 the best model information at their current configuration to compare with aircraft measurements.
216
217 The AeroCom-ATom experiment also designed three sensitivity simulations by tracking gas and
218 aerosol emissions to anthropogenic, biomass burning, and volcanic sources to attribute the origin
219 of sulfur sources on sulfur simulations over remote oceans. These experiments were conducted
220 with the Goddard Earth Observing System (GEOS) model. The setup of the GEOS model
221 followed the experiment protocol generally, but GEOS used its own daily biomass burning
222 emissions that were derived from the Quick Fire Emissions Dataset (QFED) developed based on
223 MODIS fire radiative power and calculated in near real-time at 0.1° resolution (Darmenov and
224 da Silva, 2015; Pan et al., 2020). Emissions from biogenic sources were calculated using the
225 Model for Emissions of Gases and Aerosols from Nature (MEGAN) embedded in the GEOS
226 model.
227
2.3 Tag-tracer study in GEOS

228
229 Tag trackers or tags are tied to sources of selected emission types and/or emission locations.
230 Such tag isolates plume from certain activities and is a powerful tool to help understand source
231 attribution or diagnose model performance at the process level. The mechanism behind this
232 technique is that each specific aerosol component in GEOS GOCART is modeled independently
233 of the other components, and the contribution of each emission type to the total aerosol mass is

234 not disturbed by the other emission types. Therefore, additional aerosol tracers can be easily
235 "tagged" to capture emission type (e.g., anthropogenic, biomass burning, etc.) and location
236 (local, regional or global scale). Tags can be multi-instantiated and computed simultaneously
237 with their baseline counterparts, thereby increasing the computational efficiency of the aerosol
238 models.

240 Tag-tracer technique in GEOS has been widely used in aerosol and gas studies (Bian et al., 2021;
241 Nielsen et al., 2017; Strode et al., 2018) and in supporting various aircraft field campaigns such
242 as Arctic Research of the Composition of the Troposphere from Aircraft and Satellites
243 (ARCTAS) and ATom. Such techniques are also adopted in other models such as GEOS-Chem
244 model (Fisher et al., 2017; Ikeda et al., 2017; Lin et al., 2020) and Community Earth System
245 Model (CESM, Butler et al., 2018).

247 Four tags linked to emission types of anthropogenic, biomass burning, volcanic, and marine
248 emissions were used in GEOS model to identify anthropogenic versus natural sources of sulfate,
249 and the results are discussed in Sect. 5.

251 **3. ATom-AeroCom comparisons of sulfur species**
252 This section presents a comparison of sulfur species between ATom measurements and
253 AeroCom model simulations. The consistency and diversity of data across remote regimes, both
254 horizontally and vertically, help us understand the effects of emissions, transport, and chemical
255 transformations, and shed light on improving the processes in models to best represent the ATom
256 observations.

258 **3.1 Overall comparison**
259 The overall performance of SO_4 PDF distribution observed from the AMS and PALMS
260 instruments and simulated by five AeroCom models for four ATom deployments is presented in
261 Fig. 2. Also shown in Fig. 2 are the corresponding various percentiles, namely, 0th (minimum),
262 25th, 50th (median), 75th, and 100th (maximum), and the mean for statistical analyses. The median
263 and mean values are further given in Table S1. The ATom team provided a 10-s merged dataset
264 deliberately by integrating data from various instruments to a unified temporal resolution. We
265 use this 10-s merged data where observations above detection limit (DL) throughout the main
266 text unless otherwise stated. When multiple instruments measured the target field, only points
267 where all instrument measured above DL values were included in analysis, as AMS 10-s in red
268 and PALMS 10-s in grey in Fig. 2. All model results were sampled mimicking flight
269 observations (see Sect. 2.2), and only data with measurements available were used in
270 comparison. This approach ensures that model evaluation is based on high-quality
271 measurements. It is worth noting that the given statistical values in this method represent more
272 regions having high tracer concentration or mixing ratio. In the supplementary material, we
273 further give a model-observation comparison for all available measurement data including
274 negatives.

276 The mean of PALMS SO_4 is generally about 10-50% higher than AMS SO_4 across four ATom
277 deployments. This performance may be attributed, at least in part, to the fact that the sample size
278 range of PALMS (~3 μm) is larger than that of AMS (~0.75 μm), as mentioned in Sect. 2.1.
279 However, the difference between the two observations is much smaller than the difference

280   between observation and model. Clearly, the differences in simulated SO_4 among models are
281   high and can easily exceed several orders of magnitude. Most observed and simulated SO_4
282   exhibit highest probability density around SO_4 values of 10-100 ng sm^{-3}. With the exception of
283   GEOS and CAM-ATRAS, the model SO_4 PDFs show higher tails beyond 100 ng sm^{-3}, which
284   explain the higher median and mean SO_4 simulated by the models. Statistical analysis performed
285   on selected percentiles (box-and-whisker panels in Fig. 2) indicates that multi-model SO_4
286   medians are about 3.7 (ATom-1), 2.2 (ATom-2), 1.9 (ATom-3), and 1.2 (ATom-4) times higher
287   than observed. In general, nearly all measurements and models indicate that SO_4 concentrations
288   on a global ocean basis are highest during the Northern Hemisphere (NH) spring season (ATom-
289   4). Similar analysis was also performed on all (e.g., both positive and negative) measurement
290   data (Fig. S2), the median/mean values of observations are naturally smaller than those in Fig. 2
291   by 8-20%, but the PDF distributions are almost identical between the two treatments.
292
293   Figure 3 shows the PDF distribution and statistics for SO_2. All observed and simulated data were
294   reprocessed by including points above the detection limit (2 pptv) only. Both instruments (CIMS
295   and LIF) were deployed during ATom-4. Despite CIMS being less precise than LIF (Rollins et
296   al., 2016), both instruments agreed within 95% and CIMS measured SO_2 concentrations were
297   consistently 3-7% lower than LIF measurements. This difference is within the combined
298   uncertainties of the two measurements, but it suggests a systematic calibration difference that is
299   currently unresolved (Rickly et al., 2021). Meanwhile, the width of CIMS SO_2 PDF (measured at
300   half-height) is narrower in ATom-4 than ATom-3, because of improved measurement precision
301   in ATom-4. The CIMS resolution was improved in ATom-4, which enables a better separation of
302   SO_2 and formate-H_2O. The CIMS SO_2 PDF in ATom-4 is around 10 pptv and is more consistent
303   with LIF measurements and model simulations. In contrast, the distribution of SO_2 measured by
304   CIMS during ATom-1 to -3 is spread much wider than the models. Throughout ATom periods,
305   models, especially E3SM, GEOS, and OsloCTM3, show higher peak heights and narrower peak
306   widths. Statistics indicate lower model SO_2 medians than observed (box-and-whisker in Fig. 3),
307   especially during ATom-1. However, the model means are comparable or even higher than those
308   observed, indicating that the models simulate episode events that were not reported in
309   measurements. Consequently, the simulated mean/median ratio is higher than the observed value.
310   Among the four ATom deployments, ATom-4 has much better model observation consistency.
311   Figure S3 presents the corresponding analysis, including the measured negative values.
312   Compared to Fig. 3, the observed median and mean values drop substantially (up to 50%).
313
314   Atmospheric DMS observations are scarce, especially on a global scale. Thus, DMS
315   measurements by the two instruments (WAS and TOGA) during the four ATom deployments
316   provide an unprecedented opportunity to investigate biological DMS over global remote oceans
317   and evaluate model DMS simulations on spatial and temporal distributions. By excluding points
318   with measured values below detection limit (i.e., 1 pptv), the overall DMS comparison in Fig. 4
319   indicates TOGA has higher data peaks and probability densities when DMS ranges from 3-10
320   pptv. However, this does not appear to be consistent with the lower median and mean values of
321   TOGA, indicating a higher tail in the WAS DMS PDF. Likewise, although the peak of WAS
322   DMS PDF is significantly higher than all models from 3-10 pptv (~5-20 pptv for ATom-3), the
323   median and mean of the WAS DMS are lower, suggesting an even higher tail in model DMS
324   PDF. Overall, there is a big gap between the WAS and TOGA DMS measurements, and both are
325   surprisingly low compared to the models. Statistical analysis performed on selected percentiles

326 (the box-and-whisker) indicates that multi-model DMS medians are about 4.9 (ATom-1), 8.6
327 (ATom-2), 6.6 (ATom-3), and 7.7 (ATom-4) times higher than observed, while model GEOS has
328 a better performance (i.e., 1.2, 2.7, 2.3, and 2.8 correspondingly). The model DMS median
329 values are mostly higher than the observed values. The model DMS mean values are even higher
330 than the observed means (sometimes by more than a factor of 10). This reflects a few very high
331 predicted DMS values. Based on what we know about DMS sources and sinks, these very large
332 simulated DMS appear most commonly in the boundary layer (BL). Indeed it is confirmed in Fig
333 5 by looking at the ratios of DMS median values between model simulations and observations.
334 The analyses are performed on four vertical ranges (e.g., the entire vertical column, the BL 0-1.5
335 km, the low-middle free troposphere 1.5-6 km, and the upper troposphere 6-12 km). The last
336 column "MMM/MOM" refers to multi-model median to multi-observation median. The high
337 ratio stems mostly from the BL, above which the consistency is much better. Meanwhile, the
338 PDF distribution and statistics of the models agree better with the WAS measurement than with
339 the TOGA measurement. We should also acknowledge that this is a very limited set of
340 observations we used here, and that there are some longer-term DMS observations near the
341 surface that were used as input for the parameterization of DMS emissions. More DMS
342 observations near the ocean surface are needed to make a confident comparison.
343
344 **3.2 Vertical profiles**
345 Vertical profiles of ATom-1 to -4 for observed and modeled SO_4, SO_2, DMS, and MSA are
346 shown in Figs. 6-9, respectively, for five latitude bands (from the north to the south) and for both
347 the Pacific and Atlantic Ocean basins. Again, the profiles include equal amounts of data for each
348 measurement and model result. In other words, all comparisons show only available points
349 where the two observed values (i.e., AMS vs. PALMS for SO4 and MSA, CIMS vs. LIF for
350 SO2, and TOGA vs. WAS for DMS) are greater than their detection limits, and where the model
351 values are extracted.
352
353 The average and range of sulfur tracers for ATom-1 to -4 are shown in Figs. 6-9 and their
354 corresponding details in each ATom are further given in Figs. S5-8. As shown in Fig. 6, the SO_4
355 measured by the two instruments are close to each other and lie generally within the range of
356 modelled SO_4 throughout the ATom periods. The spread of modeled SO_4 concentrations is large,
357 exceeding an order of magnitude, especially in the upper troposphere. Despite the need for
358 improvements, the models are generally able to capture the shape of the SO_4 profile.
359 Specifically, CAM-ATRAS and GEOS have good SO_4 vertical gradients over the tropical and
360 NH oceans, but their SO_4 values are too low compared to measurements over the Southern
361 Hemisphere (SH) free troposphere. The SO_4 of IMPACT and OsloCTM3 decreases too slowly
362 with altitude, as shown by their overestimated SO_4 values at high altitudes globally. The results of
363 E3SM are generally within the ranges as predicted by the other models. However, the performance of
364 these models' SO_4 vertical profiles cannot simply be explained by the way the oxidant is applied,
365 because among the five models, CAM-ATRAS, IMPACT, and OsloCTM3 used interactive
366 oxidant calculations, while E3SM and GEOS used archived oxidant data (Table 2). Of the five
367 models, OsloCTM3 and GEOS participated in the multi-model OH assessment (Nicely et al.,
368 2000) and OsloCTM3 had a shorter methane lifetime (relative to OH) than GEOS.
369
370 Figure 7 shows generally lower modeled SO_2 volume mixing ratios compared to the CIMS
371 observations for most altitudes and latitude bins. The spread among modeled SO_2 values exceeds

372 an order of magnitude around the measured SO_2. SO_2 is better simulated by model IMPACT in
373 the NH than other four AeroCom models and by models CAM-ATRAS and OsloCTM3 in the
374 SH than other three AeroCom models. The tropical Pacific appears to be an interesting region,
375 with all models except GEOS failing to capture observed local SO_2 sources. Basically, the
376 observed SO_2 is high at the surface, falls rapidly in the BL, and then gradually decreases above
377 the BL, except for ATom-1, during which a second peak appears just above the BL (see Fig. S6
378 for the details of ATom-1 to -4 separately). These observations indicate a strong local source for
379 SO_2 in all seasons and a transport source in the low free-troposphere NH summer (ATom-1).
380 Like observations, the model GEOS predicts a local source for SO_2 at the surface, but it misses
381 the plume above the BL in ATom-1, and its vertical SO_2 convection is consistently too weak.
382 Since only one flight was in ATom-1, more observations are needed to confirm whether GEOS
383 has been failing to catch the plume there during the NH summer. All other models show lower
384 SO_2 at the surface than in the lower free troposphere, which is inconsistent with the observed
385 profiles. Figure S6 also shows an excellent agreement of SO_2 profiles measured by the CIMS and
386 LIF during ATom-4 and models agree with measurements better in ATom-4 as well.
387
388 DMS measurements fill in another piece of the puzzle for the atmospheric sulfur budget. As
389 shown in Fig. 8, all five AeroCom models generally overestimate DMS in the BL, particularly
390 for models CAM-ATRAS and OsloCTM3. This large bias close to the surface requires us to
391 revisit the DMS emissions employed in our models. Of the five models, DMS emissions of
392 E3SM, and IMPACT are derived directly from climate emission inventories, while the DMS
393 emission of the other three models are parameterized using monthly climatological DMS
394 concentrations in sea water and surface meteorologies (e.g. surface wind and temperature, see
395 details in Table 3). Specifically, the parameterization used to convert DMS seawater
396 concentrations into DMS emission fluxes was using Nightingale et al. (2000) in CAM-ATRAS
397 and OsloCTM3 and Liss and Merlivat (1986) in GEOS. The three models used two inventories
398 of monthly DMS seawater concentrations, Lana et al. (2011) for CAM-ATRAS and GEOS, and
399 Kettle and Andreae (2000) for OsloCTM3. It is worth noting that even the latest climatological
400 database by Lana et al. (2011) was constructed by compiling measurements before 2000, so the
401 potential long-term change of DMS emission caused by environment change could be missed
402 (Barford, 2013). Also, although the data set used by Lana et al. (2011) is large (i.e., ~47,000
403 seawater concentration measurements), interpolation and extrapolation techniques were still
404 necessary in creating a global monthly climatological DMS emission. Gali et al. (2018) reported
405 updated oceanic DMS levels on a global scale using remote sensing satellite data. However,
406 much effort is still needed to accurately establish global rates of change in order to create global
407 DMS emissions for climate modeling. This parameterization of air-sea exchange is important
408 because CAM-ATRAS and OsloCTM3, using the same parameterization but different DMS
409 seawater concentrations, reported close emissions in Table 4. On the other hand, the DMS
410 emissions of CAM-ATRAS are almost twice as high as those of GEOS. This difference in
411 emissions results from different parameterizations in the two models, since both models read the
412 same DMS seawater concentration.
413
414 Meanwhile, the modeled DMS vertical gradient is generally steeper than the observed one (e.g.,
415 Fig. 8 A54N-90N), implying slower vertical transport or faster chemical conversion of DMS to
416 SO_2 in the model. The data submitted by the AeroCom models did not provide us with enough
417 information to obtain the determinants. Currently, GEOS and OsloCTM3 account for two

418 products from the oxidation of DMS (i.e., SO_2 and MSA) but only GEOS output MSA results.
419 The other models consider DMS oxidation products only as SO_2. These chemical processes in
420 the model may also need to be revisited. Previous studies proposed other chemical reactions for
421 DMS loss in the atmosphere. For example, halogen chemistry represented 71% of the DMS loss
422 in the study of Hoffmann et al. (2016). Veres et al. (2020) estimated that about 30% of DMS in
423 the atmosphere was oxidized to hydroperoxymethyl thioformate (HPMTF), reported only in
424 ATom-4. To this end, the HPMTF serves as a new reservoir of oceanic sulfur and its life cycle in
425 the atmosphere is unknown. The new finding indicates that important components of Earth's
426 sulfur cycle are not yet been fully understood and urges us to reassess this fundamental marine
427 chemical cycle. However, including these chemical DMS losses further reduces DMS above the
428 surface, making DMS in the models even lower at high altitudes.
429
430 The GEOS MSA matches observations (Fig. 9) in the lower troposphere. In the upper
431 troposphere (UT), the GEOS MSA tends to decrease slowly or even increase with altitude. These
432 patterns do not agree with observations, and this inconsistency can be explained at least partially
433 by the MSA gas-aerosol partitioning defined in the model and observations. AMS and PALMS
434 only measure the particle phase of MSA, but GEOS MSA is the total MSA and is not accurately
435 represented by observations, especially in UT. Yan et al. (2019) reported that the ratio of MSA to
436 SO_4 can be reduced by 30% when calculations do not consider methanesulfonic acid in the gas
437 phase (MSAg) at low temperatures.
438
439 **3.3 Regional and seasonal analysis**
440 In order to analyze model performance on a regional and seasonal basis, Figs. 10-12 show
441 histograms of SO_4, SO_2, and DMS concentrations as a function of altitude (rows) and latitudinal
442 band (columns). Only multi-model median is shown here to highlight any common problems in
443 the models. Further details of each individual model are given in Figs. S9-11 and discussed in
444 supplementary material. Each model in this study has its bias at a specific time and location.
445 With the information provided by Figs. S9-11, modelers can further explore the simulation to
446 identify potential causes of model anomalies.
447
448 High SO_4 concentration regions vary across seasons (Fig. 10). In the free troposphere (i.e., 1.5 –
449 12 km), these regions cover the tropics to mid-latitudes in summer and winter (i.e., ATom-1 and
450 ATom-2) and shift to mid- to high-latitudes in spring and autumn (i.e., ATom-3 and ATom-4).
451 The areas with the highest concentration appeared in the SH high-latitudes during ATom-3 (SH
452 spring) and the NH high-latitudes during ATom-4 (NH spring). In the BL, the tropical
453 atmospheric SO_4 concentration appears to be always elevated, and SO_4 concentration levels and
454 SO_4 interregional variation are more pronounced in ATom-1 (NH summer). Among all AToms,
455 the performance of the model SO_4 simulation is best for ATom-4 and worst for ATom-1 (NH
456 summer). Compared to observations, model tends to simulate higher SO_4 concentrations in the
457 free troposphere. Both observations and simulations show that the SO_4 over the Pacific is higher
458 than that over the Atlantic during the NH high-latitude autumn (ATom-3) and the NH mid-
459 latitude spring (ATom-4). The differences between observations and simulations are generally
460 larger in the Atlantic than in the Pacific, particularly in the SH. SO_4 concentration levels in
461 simulations and observations can differ significantly in certain areas of each ATom. Differences
462 may be caused by majority models or a few individual models. For example, in summer and
463 winter, the CAM-ATRAS model gave the highest estimates of atmospheric SO_4 in the oceanic

464 BL, but the IMPACT and OsloCTM3 models gave the highest estimates of atmospheric SO_4 in
465 the free troposphere (Fig. S9). All models except the GEOS model generally overestimate SO_4 in
466 the atmosphere.
467
468 Atmospheric SO_2 (Fig. 11) is most abundant in the BL of NH mid-latitude Pacific Ocean during
469 ATom-1 (NH summer) and the tropical Pacific BL during ATom-3 (NH autumn), and this high
470 SO_2 region extends to the atmosphere above. Areas where free tropospheric SO_2 concentrations
471 are relatively large do not necessarily follow the example of the BL. For instance, free
472 troposphere appears to be more polluted than other regions in the NH Pacific during ATom-2
473 and in the SH mid-latitude Atlantic (A40S-20S) during ATom-4, but not in the BL, implying a
474 potential source of SO2 by horizontal transport. The interregional variation of SO_2 in BL is much
475 larger than in the free troposphere, from which local oceanic sources of SO_2 can be inferred. In
476 terms of model-observation comparison, model simulated SO_2 in the free troposphere is
477 generally lower, which is opposite to the case of SO_4. A rapid SO_2 to SO_4 chemical conversion in
478 models could be one of reasons. Fig. S10 further shows individual model SO_2 simulation. For
479 example, the E3SM model gives significantly higher SO_2 compared with the measurements and
480 other models in BL (Fig. S10). Unlike the case of SO_4, all models tend to underestimate SO_2 in
481 the free troposphere, with some exceptions, such as the GEOS model for the mid- to high-
482 latitude North Pacific winter (ATom-2) and the CAM-ATRAS and IMAPCT models for the mid-
483 latitude South Atlantic autumn (ATom-4).
484
485 Surface DMS (Fig. 12) is generally higher in the tropics when the ocean is warm and in mid-high
486 latitudes during springtime (e.g., ATom-3 SH spring and ATom-4 NH spring). A remarkable
487 pattern of high model DMS values in the BL is revealed throughout the ATom cycle. This
488 phenomenon also occurs in the free lower troposphere, but not necessarily in the upper
489 troposphere. The high model DMS in BL can be attributed to (1) too high DMS emission, (2) too
490 slow DMS chemical loss, and (3) too slow DMS vertical transport from BL to free troposphere.
491 Additional insight can be obtained by focusing on remote high-latitudes, for example SH high-
492 latitude (40°S-70°S) Pacific, where land source impacts are limited. Thus, the higher simulated
493 SO_2 there in the BL in SYom-4 ruled out a chemical cause due to low DMS loss. The extremely
494 high surface DMS is also not due to the slow vertical transport because simulated DMS is also
495 high in the layers above the BL. A large model DMS emission is likely responsible for the
496 simulated high surface DMS. The overestimation of surface DMS multi-model median in Fig. 12
497 is clearly attributable to the contribution of all models shown in Fig. S11, with the models CAM-
498 ATRAS and OsloCTM3 being more prominent.
499
500 **4. Sulfur budget from AeroCom models**
501 Budget analysis is a simple and basic method that has been widely used to document the
502 underlying performance of a model. This analysis allows us to evaluate the AeroCom-III sulfur
503 simulations against previous AeroCom-I and -II studies and serves as a record for future model
504 evaluations. Table 4 summarizes the global sulfur budgets for emissions, wet/dry deposition and
505 chemistry from the five models. Clearly, the largest source of sulfur (~70 TgS/yr) is SO_2 emitted
506 directly from anthropogenic (~78%), biomass burning (~2%), and volcanic sources (~20%).
507 Biogenic DMS (~15-30 TgS) produced and outgassed from decomposition of marine organic
508 molecules provides the largest natural source of sulfur to the atmosphere. A small amount of SO_4
509 (< 3%) is emitted directly from anthropogenic sources.

510
511   DMS is oxidized in the atmosphere by OH and NO_3 radicals to form SO_2 and MSA. This
512   biological source of SO_2, along with SO_2 emitted directly from other sources, reacts with
513   hydroxyl radicals (OH) in the gas phase and hydrogen peroxide (H_2O_2) and ozone (O_3) in the
514   aqueous phase to produce sulfuric acid (H_2SO_4) and eventually sulfate particles, which play an
515   important role in the formation of clouds over the oceans.
516
517   In the five models, DMS predicts the shortest global average lifetime (0.6-2.0 days), followed by
518   SO_2 (1.1-1.8 days), and SO_4 the longest lifetime (3.1-5.6 days). Among them, GEOS has the
519   lowest global burden and shortest lifetime for all sulfur species. The magnitudes of global
520   burdens and lifetimes shown here support the model performance shown in Figs. 2-8. For
521   example, models CAM-ATRAS and OsloCTM3 predicts the highest DMS emission, which is
522   consistent with the highest DMS value (Fig. 4 and S11) and longest lifetime simulated by the
523   two models.
524
525   The key budget items include DMS emission, SO_2 emission, sulfate source or total deposition
526   (source and deposition are pretty much the same as expected), lifetime (inversely proportional to
527   the loss rate), and total atmospheric mass load. From the multi-model mean and standard
528   deviation, the diversity can be calculated. Figure 13 shows the global mean budget items in the
529   percentage deviation of each model from the multi-model mean, following the same concept
530   shown in Schulz et al. (2006) and Gliss et al. (2021). It reveals the processes causing model
531   differences. For example, E3SM and GEOS have approximately the same SO_2 emissions and
532   total sulfate sources, but the sulfate lifetime is much shorter in GEOS (implying faster removal
533   rates) thus smaller sulfate burden that is consistent with lower sulfate concentrations in GEOS
534   than in E3SM. At the same time, the lower total sulfate source in E3SM is compensated by
535   longer lifetime compared to CAM-ATRAS, resulting in a comparable global burden of SO_4 in
536   the two models.
537
538   It is worth pointing out that the much lower atmospheric SO_4 mass loading of the GEOS
539   simulations is not necessarily related to the poor performance of the GEOS SO_4 simulations, as
540   revealed by the model-measurement comparison in Figs 2, 6 and S9. Although the multi-model
541   mean (or median) often represents the best predictor in the modeling domain, common modeling
542   problems or too small model sample can compromise this effort.
543
544   To date, there have been no sulfur budget reports focusing on the vast ocean. However, previous
545   AeroCom studies have reported global sulfate atmospheric loading and its diversity across
546   multiple AeroCom models using monthly and global mean column loadings. Table 5 summarizes
547   these studies, including their reported global and annual sulfate multi-model mean (MMM) and
548   diversity (δ). δ is related to the standard deviation (std_dev) and is defined as δ = std_dev /
549   MMM *100 (%). The results of this work are lower than AeroCom-I but higher than AeroCom-
550   II, which may be related to the different target years involved in these studies. One point to note
551   is that the diversity δ of AeroCom-III models has not reduced since AeroCom-I, which was
552   studied nearly 20 years ago.
553
554   **5. Source origins for aerosol SO_4 along flight track and Ocean basins**

555   In this section, we perform an analysis of source attribution by tagging the sulfur source types
556   using the GEOS model. This model is the only one that provides tagged data. Our goal is to
557   understand the sources (anthropogenic, biological, volcanic) of sulfate aerosols in remote regions
558   and how chemistry, transport, and removal processes determine the vertical distribution of
559   sulfate aerosols across seasons and ocean locations.
560

561   Figure 14a presents a quantitative summary of the source attribution of aerosol SO_4 sampled
562   along the ATom flight tracks. The analysis was performed over four seasons, spanning the
563   troposphere and three vertical layers (i.e., marine boundary layer, free troposphere and upper
564   troposphere). Overall, anthropogenic emissions were the dominant source (40–60% of the total)
565   of simulated tropospheric SO_4 along the ATom flight tracks for almost all altitudes and seasons,
566   followed by volcanic (18–32%) and oceanic sources (16–32%). Anthropogenic pollution
567   prevailed over remote oceans most in spring and autumn (ATom-3 and -4). The overall
568   contributions from volcanic and oceanic sources are comparable during the ATom periods.
569   Meanwhile, the ocean source contribution has an obvious seasonal variation which is most active
570   during the SH summer (ATom-2), when marine biochemical activity in the vast Southern Ocean
571   is the largest. Volcanos show the largest contribution in the NH summer 2016 (ATom-1) during
572   the four ATom deployments. Given the irregular character of eruptions, the volcanic contribution
573   deserves further discussion below.
574

575   In the vertical direction, SO_4 from anthropogenic emissions contributes more than 50% to the
576   free to upper troposphere. Even in the marine boundary layer, anthropogenic sources of SO_4 still
577   account for the largest fraction, except in the SH summer (ATom-2) when oceanic source
578   became dominant. The relative importance of volcanic and marine sources varies not only
579   seasonally but also vertically. Oceanic sources understandably make up a significant fraction
580   (26-42%) of SO_4 in the boundary layer. In the free troposphere, their contribution drops off
581   sharply, reflecting their local surface source characteristics. On the other hand, SO_4 from
582   anthropogenic emissions (including shipping emission) expands in the free troposphere,
583   suggesting that the source originated from distant continental areas. Volcanic SO_4 remains nearly
584   constant throughout the troposphere, making volcanoes the second largest source there.
585   Meanwhile, the contribution of others (OTH including biomass burning) to remote ocean SO_4 is
586   relatively small (< 3%) and will not be discussed further in this study.
587

588   The sources of SO_4 discussed above are deduced from the location and timing of the ATom
589   flight path. Conclusions about the total contribution of the ocean needs caution, as there may be
590   representativeness issues using such narrow-band and instantaneous sampling. There might be a
591   situation where, for example, volcanoes provide a very large signal but only account for a small
592   measured area, and in most regions, volcanoes play a very minor role. Whereas oceanic sources
593   in the marine boundary layer perhaps were the dominant source for a much wider region, the SO_4
594   concentration resulting from the DMS was overall a smaller amount compared to other sources
595   where near a volcanic or anthropogenic source. To address this representation issue, we perform
596   one more analysis with the model data averaged over a wider oceanic region (the shaded area in
597   Fig. 1) and over a longer period (i.e., monthly mean over ATom periods). Such source
598   attributions are given in Fig. 14b.
599

Qualitative conclusions drawn from source attribution along the flight tracks generally apply to the ocean basin source attribution, albeit to a slightly different extent. This confirms that continental man-made sources dominate tropospheric SO_4 even over oceans. There is a clear seasonal variation in oceanic contribution, which is largest in austral summer (ATom-2) followed by boreal summer (ATom-1). Concerning volcanic sources, emissions from volcanoes are of two types. One type is the volcanic degassing emissions that tend to remain nearly constant throughout the year and are equivalent to about 20% of SO_2 global anthropogenic emissions. This degassing emission ensures that volcanoes contribute more than 20% to SO_4 over the oceans. The other type consists in the volcanic eruptions. Due to the irregularity of volcanic eruptions in terms of different eruption locations, magnitudes, and times, volcanic eruptions can cause severe fluctuations in SO_4 in the atmosphere. Compared with the source attribution along the flight trajectory, the volcanic contribution decreased over a larger spatial and temporal domain (i.e., ocean basin and monthly mean) in the NH winter 2017 by 32% (ATom-2) and increased in all other three seasons by 14-33%, especially in the NH spring 2018 (ATom-4), when the massive Kilauea eruption in Hawaii began on 3 May 2018. Contrarily, the anthropogenic contribution increased in the NH winter (ATom-2) by 5% and decreased in other seasons by 7-21%.

6. Conclusions
This study investigates sulfur species in remote tropospheric regions at global and seasonal scales using airborne ATom measurements and AeroCom models. The goal is to understand the atmospheric sulfur cycle over the remote oceans, each model's behavior and the spread of model simulations, as well as the observation-model discrepancies. Such understanding and comparison with real observations are crucial to narrow down the uncertainty in model sulfur simulation. Even after decades of development, models are still struggling to accurately simulate sulfur distributions, with differences between models often exceeding an order of magnitude. On the other hand, the agreement between instruments is usually much better. Differences between modeled SO_4 are particularly large in the tropical upper troposphere, where deep convective transport allows a small portion of sulfur to reach the lower stratosphere where sulfate aerosols can persist for many years. Compared with observations, simulated SO_2 is generally low while SO_4 is high. Modeled DMS values are typically an order of magnitude higher than observed DMS near the surface, pointing to a need to revisit the DMS emission inventories and/or the biogeochemical modules used to predict DMS emissions. Our work also suggests investigating three other potential corresponding processes to improve sulfur simulation: whether the chemical conversion from SO_2 to SO_4 is too rapid, whether DMS-generated free tropospheric SO_2 is too low, and whether the vertical transport of DMS and SO_2 from BL to free troposphere is too low. This further investigation requires atmospheric oxidant fields and the ability to track SO_2 production and loss using tagged tracers.

We investigate source attribution of SO_4 over remote oceans seasonally and vertically. Sampled at the location and time of ATom measurements, anthropogenic emissions were the dominant source (40–60% of the total) of simulated tropospheric SO_4 at almost all heights and seasons, followed by volcanic (18–32%) and oceanic sources (16–32%). These contributions changed to 34–56%, 17–37%, and 19–37% when extended to the broad Pacific and Atlantic during the months of ATom deployment. This survey confirms that anthropogenic sources dominate tropospheric SO_4 even over oceans. Given that we find DMS source to be overestimated in the

646 models, the anthropogenic sources overall are a larger portion of the budget, and biogenic is
647 likely smaller than volcanic. Volcanic degassing throughout the year contributes about 20%, and
648 this proportion is increased by explosive eruptions that vary in location and timing. The oceanic
649 contribution has obvious seasonal variation, the largest in the Southern Hemisphere summer,
650 followed by the Northern Hemisphere summer.
651
652 It is understood that anthropogenic sulfur emissions currently offset a significant portion of
653 greenhouse gas warming, but they are rapidly declining through emissions controls. As these
654 anthropogenic emissions decrease, natural sources of sulfur, particularly bio-derived sulfur
655 compounds discharged from the world's oceans, will increase their relative contribution.
656 Therefore, more efforts are needed to understand the sulfur cycle in remote environments. On the
657 other hand, our study is the first asserting that anthropogenic emissions remain a major source of
658 sulfate aerosols generated over remote oceans during the ATom deployment periods, suggesting
659 that any limitation of anthropogenic sulfur emissions would have modern global implications.
660
661 Even after two decades of development, the diversity of sulfate simulations from AeroCom-I to
662 AeroCom-III has not decreased. However, accurate sulfate simulation in current climate models
663 is crucial to reduce radiative forcing biases. More importantly, apart from the shortcomings of
664 individual models, all modelers involved in this work should focus on the calculation of the air-
665 sea exchange flux formula as it plays a key role in determining DMS emissions. To our
666 knowledge, many other aerosol models employ similar formulas in air-sea flux calculations, so
667 the findings here are applicable to them as well. Modelers also need to study DMS and SO_2
668 vertical transport as well as SO_4 wet deposition during long-distance transport, as model biases
669 are greatest at high altitudes. One suggestion to modelers is that the use of online oxidant fields
670 is insufficient to explain the model sulfate bias, as there was no systematic bias in the sulfate
671 simulations between the models using interactive oxidants and the models using archival
672 oxidants in this study. The complexity of chemistry deserves more attention.
673
674 *Code availability.* The GEOS Earth System Model source code and the instructions for model build are available
675 at https://github.com/GEOS-ESM/GEOSgcm/ (Last accessed: 28 August 2023).
676
677 *Data availability.* The AeroCom model outputs needed to reproduce the results described in this paper are
678 publicly available for download at https://acd-ext.gsfc.nasa.gov/anonftp/acd/tropo/bian/ATom-AeroCom-Sulfur/.
679 The ATom data was obtained from their ESPO Data Archive: https://espo.nasa.gov/atom/content/ATom, last
680 accessed: 28 August 2022.
681

682 *Author contributions.*
683 BH and MC conceptualized ATom-AeroCom experiment. BH performed analysis and wrote the manuscript. BH,
684 PRC, MLi, MTL, RBS, HM, JEP, HW, KZ, and JZ provided AeroCom model results and ECA, KF, RSH, JJ, PCJ,
685 MLa, BAN, AWR, GS, and LX contributed to ATom measurements. All authors contributed to the editing of the
686 manuscript.

687
688 *Competing interests.*
689 At least one of the co-authors is a member of the editorial board of Atmospheric Chemistry and Physics.
690

691 *Acknowledgements.*
692 HB, MC, and PRC acknowledge the GEOS model developmental efforts at Global Modeling and Assimilation
693 Office (GMAO). This work was supported by NASA's Aura STM and ISFM programs and ACMAP award

694 (80NSSC23K1000). The computing resources supporting this work were provided by the NASA High-End
695 Computing (HEC) Program through the NASA Center for Climate Simulation (NCCS).
696 ECA and RSH acknowledge the support of the National Center for Atmospheric Research, which is a major facility
697 sponsored by the National Science Foundation under Cooperative Agreement No. 1852977.
698 MLi acknowledges the support of JSPS Postdoctoral Fellowships for Research in Japan (Standard).
699 HM was supported by the Ministry of Education, Culture, Sports, Science, and Technology and the Japan Society
700 for the Promotion of Science (MEXT/JSPS) KAKENHI grants (JP19H05699, JP19KK0265, JP20H00196,
701 JP20H00638, JP22H03722, JP22F22092, JP23H00515, JP23H00523, and JP23K18519); by the MEXT Arctic
702 Challenge for Sustainability II (ArCS II) project (JPMXD1420318865); and by the Environment Research and
703 Technology Development Fund 2-2003 (JPMEERF20202003) and 2-2301 (JPMEERF20232001) of the
704 Environmental Restoration and Conservation Agency.
705 KZ and HW acknowledge support by the U.S. Department of Energy (DOE), Office of Science, Office of Biological
706 and Environmental Research, Earth and Environmental Systems Modeling program. The Pacific Northwest National
707 Laboratory (PNNL) is operated for DOE by Battelle Memorial Institute under contract DE-AC05-76RLO1830.
708 LX thanks Michelle Kim, Hannah Allen, John Crounse, and Paul Wennberg for operating the Caltech CIMS
709 instrument during ATom. LX acknowledges NASA grant NNX15AG61A.
710 MTL thanks Marit Sandstad (CICERO) for assistance with the model post-processing and acknowledges
711 the National Infrastructure for High Performance Computing and Data Storage in Norway (UNINETT) resources
712 (grant NN9188K).
713 RBS acknowledges funding from the Research Council of Norway (grant number 314997).

714

References

716 Abdul-Razzak, H. and Ghan, S.: A parameterization of aerosol acivation, 2. Multiple aerosol
717 types, J. Geophys. Res. Atmos., 105, 6837–6844, https://doi.org/10.1029/1999JD901161, 2000.

718 Allen, H. M., Bates, K. H., Crounse, J. D., Kim, M. J., Teng, A. P., Ray, E. A., and Wennberg, P.
719 O.: H_2O_2 and CH_3OOH (MHP) in the Remote Atmosphere: 2. Physical and Chemical Controls,
720 J. Geophys. Res. Atmos., 127, e2021JD035702, https://doi.org/10.1029/2021JD035702, 2022.

721 Bacmeister, J., Suarez, M., and Robertson, F. R.: Rain Reevaporation, Boundary-Layer,
722 Convection Interactions, and Pacific Rainfall Patterns in an AGCM, J. Atmos. Sci., 63, 3383–
723 3403, https://doi.org/10.1175/JAS3791.1, 2006.

725 Barahona, D. and Nenes, A.: Parameterizing the competition between homogeneous and
726 heterogeneous freezing in cirrus cloud formation – monodisperse ice nuclei, Atmos. Chem.
727 Phys., 9, 369–381, https://doi.org/10.5194/acp-9-369-2009, 2009.

729 Barahona, D., Molod, A., Bacmeister, J., Nenes, A., Gettelman, A., Morrison, H., Phillips, V.,
730 and Eichmann, A.: Development of two-moment cloud microphysics for liquid and ice within
731 the NASA Goddard Earth Observing System Model (GEOS-5), Geosci. Model Dev., 7, 1733–
732 1766, https://doi.org/10.5194/gmd-7-1733-2014, 2014.

734 Barford, E.: Rising ocean acidity will exacerbate global warming, Nature,
735 https://doi.org/10.1038/nature.2013.13602, 2013.

737 Bian, H., Luo, C., and Li, X.: Numerical modeling of air pollutant and rainfall effect on acid wet
738 deposition, ACTA Meteorol. Sin., 7, 3, 273–286, 1993.

740 Bian, H., Chin, M., Hauglustaine, D. A., Schulz, M., Myhre, G., Bauer, S. E., Lund, M. T.,
741 Karydis, V. A., Kucsera, T. L., Pan, X., Pozzer, A., Skeie, R. B., Steenrod, S. D., Sudo, K.,

742   Tsigaridis, K., Tsimpidi, A. P., and Tsyro, S. G.: Investigation of global nitrate from the
743   AeroCom Phase III experiment, Atmos. Chem. Phys., 17, 12911–12940,
744   https://doi.org/10.5194/acp-17-12911-2017, 2017.
745
746   Bian, H., Froyd, K., Murphy, D. M., Dibb, J., Darmenov, A., Chin, M., Colarco, P. R., da Silva,
747   A., Kucsera, T. L., Schill, G., Yu, H., Bui, P., Dollner, M., Weinzierl, B., and Smirnov, A.:
748   Observationally constrained analysis of sea salt aerosol in the marine atmosphere, Atmos. Chem.
749   Phys., 19, 10773–10785, https://doi.org/10.5194/acp-19-10773-2019, Aug., 2019.
750
751   Bian, H., Lee, E., Koster, R. D., Barahona, D., Chin, M., Colarco, P. R., Darmenov, A.,
752   Mahanama, S., Manyin, M., Norris, P., Shilling, J., Yu, H., and Zeng, F.: The response of the
753   Amazon ecosystem to the photosynthetically active radiation fields: integrating impacts of
754   biomass burning aerosol and clouds in the NASA GEOS Earth system model, Atmos. Chem.
755   Phys., 21, 14177–14197, https://doi.org/10.5194/acp-21-14177-2021, 2021.
756
757   Boucher, O., Randall, D., Artaxo, P., Bretherton, C., Feingold, G., Forster, P., Kerminen, V.-M.,
758   Kondo, Y., Liao, H., Lohmann, U., Rasch, P., Satheesh, S., Sherwood, S., Stevens, B., and
759   Zhang, X.: in: Climate Change 2013: The Physical Science Basis, in: Contribution of Working
760   Group I to the Fifth Assessment Report of the Intergovernmental Panel on Climate Change:
761   Clouds and Aerosols, edited by: Stocker, T., Qin, D., Plattner, G.-K., Tignor, M., Allen, S.,
762   Boschung, J., Nauels, A., Xia, Y., Bex, V., and Midgley, P., Cambridge University Press,
763   Cambridge, UK and New York, NY, USA, 571–657, 2013.
764
765   Breen, K. H., Barahona, D., Yuan, T., Bian, H., and James, S. C., Effect of volcanic emissions on
766   clouds during the 2008 and 2018, Atmos. Chem. Phys., 21, 7749–7771,
767   https://doi.org/10.5194/acp-21-7749-2021, 2021.
768
769   Brock, C. A., Williamson, C., Kupc, A., Froyd, K. D., Erdesz, F., Wagner, N., Richardson, M.,
770   Schwarz, J. P., Gao, R.-S., Katich, J. M., Campuzano-Jost, P., Nault, B. A., Schroder, J. C.,
771   Jimenez, J. L., Weinzierl, B., Dollner, M., Bui, T., and Murphy, D. M.: Aerosol size distributions
772   during the Atmospheric Tomography Mission (ATom): methods, uncertainties, and data
773   products, Atmos. Meas. Tech., 12, 3081–3099, 2019.
774
775   Butler, T., Lupascu, A., Coates, J., and Zhu, S.: TOAST 1.0: Tropospheric Ozone Attribution of
776   Sources with Tagging for CESM 1.2.2, Geosci. Model Dev., 11, 2825–2840,
777   https://doi.org/10.5194/gmd-11-2825-2018, 2018.
778
779   Carn, S. A., Clarisse, L., and Prata, A. J.: Multi-decadal satellite measurements of global
780   volcanic degassing, J. Volcanol. Geotherm. Res., 311, 99–134,
781   http://dx.doi.org/10.1016/j.jvolgeores.2016.01.002, 2016.
782
783   Carn, S. A., Fioletov, V. E., McLinden, C. A., and Krotkov, N. A.: A decade of global volcanic
784   SO_2 emissions measured from space, Sci. Rep., 7, 44095, https://doi.org/10.1038/srep44095,
785   2017.
786

787 Chin, M., Rood, R. B., Lin, S. J., Müller, J.-F., and Thompson, A. M.: Atmospheric sulfur cycle
788 simulated in the global model GOCART: model description and global properties, J. Geophys.
789 Res. Atmos., 105, D20, 24671–24687, https://doi.org/10.1029/2000JD900384, 2000.
790
791 Colarco, P. R., da Silva, A., Chin, M., and Diehl, T.: Online simulations of global aerosol
792 distributions in the NASA GEOS-4 model and comparisons to satellite and ground-based aerosol
793 optical depth, J. Geophys. Res. Atmos., 115, D14207, https://doi.org/10.1029/2009JD012820,
794 2010.
795
796 Crounse, J. D., McKinney, K. A., Kwan, A., J. and Wennberg, P. O., Measurement of Gas-Phase
797 Hydroperoxides by Chemical Ionization Mass Spectrometry, Anal. Chem., 78, 19, 6726–6732,
798 https://doi.org/10.1021/ac0604235, 2006.
799
800 Darmenov, A. and da Silva, A.: The Quick Fire Emissions Dataset (QFED) - Documentation of
801 versions 2.1, 2.2 and 2.4, NASA TM-2015-104606, Vol. 38, 183 pp., 2015.
802
803 Dentener, F., et al. (2006). "Emissions of primary aerosol and precursor gases in the years 2000
804 and 1750 prescribed data-sets for AeroCom." Atmospheric Chemistry and Physics 6: 4321-4344.
805
806 Dong, X., Fu, J. S., Zhu, Q., Sun, J., Tan, J., Keating, T., Sekiya, T., Sudo, K., Emmons, L.,
807 Tilmes, S., Jonson, J. E., Schulz, M., Bian, H., Chin, M., Davila, Y., Henze, D., Takemura, T.,
808 Benedictow, A. M. K., and Huang, K.: Long-range transport impacts on surface aerosol
809 concentrations and the contributions to haze events in China: an HTAP2 multi-model study,
810 Atmos. Chem. Phys., 18, 15581-15600, https://doi.org/10.5194/acp-18-15581-2018, 2018.
811
812 Eger, P. G., Helleis, F., Schuster, G., Phillips, G. J., Lelieveld, J., and Crowley, J. N.: Chemical
813 ionization quadrupole mass spectrometer with an electrical discharge ion source for atmospheric
814 trace gas measurement, Atmos. Meas. Tech., 12, 1935–1954, https://doi.org/10.5194/amt-12-
815 1935-2019, 2019.
816
817 Feng, L., Smith, S. J., Braun, C., Crippa, M., Gidden, M. J., Hoesly, R., Klimont, Z., van Marle,
818 M., van den Berg, M., and van der Werf, G. R.: The generation of gridded emissions data for
819 CMIP6, Geosci. Model Dev., 13, 461–482, https://doi.org/10.5194/gmd-13-461-2020, 2020.
820
821 Fisher, J. A., Murray, L. T., Jones, D. B. A., and Deutscher, N. M.: Improved method for linear
822 carbon monoxide simulation and source attribution in atmospheric chemistry models
823 illustrated using GEOS-Chem v9, Geosci. Model Dev., 10, 4129–4144,
824 https://doi.org/10.5194/gmd-10-4129-2017, 2017.
825
826 Fountoukis, C. and Nenes, A.: Continued development of a cloud droplet formation
827 parameterization for global climate models, J. Geophys. Res. Atmos., 110, D11212,
828 https://doi.org/10.1029/2004JD005591, 2005.
829
830 Fricko O., Havlik P., Rogelj J., Klimont Z., Gusti M., Johnson N., Kolp P., Strubegger M., Valin
831 H., Amann M., Ermolieva, T., Forsell, N., Herrero, M. , Heyes, C., Kindermann, G.,
832 Volker Krey, V., McCollum, D. L., Obersteiner, M., Shonali Pachauri, S., Shilpa Rao, S., Riahi,

K., The marker quantification of the Shared Socioeconomic Pathway 2: a middle-of-the-road scenario for the 21st century. Glob. Environ. Change, 42, 251–267, 2017.

Froyd, K. D., Yu, P., Schill, G. P., Brock, C. A., Kupc, A., Williamson, C. J., Jensen, E. J. Ray, E., Rosenlof, K. H., Bian, H., Darmenov, A. S., Colarco, P. R., Diskin, G. S., Bui, T. P., and Murphy, D. M., Global-scale measurements reveal cirrus clouds are seeded by mineral dust aerosol, Nat. Geosci., Volume 15, Issue 3, p.177-183, 10.1038/s41561-022-00901-w, Feb, 2022.

Fung K. M., Heald, C.L., Kroll, J.H., Wang, S., Jo, D.S., Gettelman, A., Lu, Z., Liu, X., Zaveri, R. A., Apel, E. C., Blake, D., R., Jimenez, J., Campuzano-Jost, P., Veres, P. R., Bates, T. S.,Shilling, J. E., and Zawadowicz. M., Exploring dimethyl sulfide (DMS) oxidation and implications for global aerosol radiative forcing. Atmos. Chem. and Phys., 22, 2:1549-1573, PNNL-SA-166358, https://doi:10.5194/acp-22-1549-2022, 2022.

Galí, M., Levasseur, M., Devred, E., Simó, R., and Babin, M.: Sea-surface dimethylsulfide (DMS) concentration from satellite data at global and regional scales, Biogeosciences, 15, 3497–3519, https://doi.org/10.5194/bg-15-3497-2018, 2018.

Gao, C. Y., Heald, C. L., Katich, J. M., Luo, G., Yu, F., Remote Aerosol Simulated During the Atmospheric Tomography (ATom) Campaign and Implications for Aerosol Lifetime, J. Geophys. Res. Atoms., Vol. 127, I. 22, https://doi.org/10.1029/2022JD036524, 2022.

Gliß, J., Mortier, A., Schulz, M., Andrews, E., Balkanski, Y., Bauer, S. E., Benedictow, A. M. K., Bian, H., Checa-Garcia, R., Chin, M., Ginoux, P., Griesfeller, J. J., Heckel, A., Kipling, Z., Kirkevåg, A., Kokkola, H., Laj, P., Le Sager, P., Lund, M. T., Lund Myhre, C., Matsui, H., Myhre, G., Neubauer, D., van Noije, T., North, P., Olivié, D. J. L., Rémy, S., Sogacheva, L., Takemura, T., Tsigaridis, K., and Tsyro, S. G.: AeroCom phase III multi-model evaluation of the aerosol life cycle and optical properties using ground- and space-based remote sensing as well as surface in situ observations, Atmos. Chem. Phys., 21, 87–128, https://doi.org/10.5194/acp-21-87-2021, Jan., 2021.

Grennfelt, P., Engleryd, A., Forsius, M., Hov, Ø., Rodhe, H., and Cowling, E.: Acid rain and air pollution: 50 years of progress in environmental science and policy, Ambio, 49, 849–864, https://doi.org/10.1007/s13280-019-01244-4, 2020.

Gryspeerdt, E., Povey, A. C., Grainger, R. G., Hasekamp, O., Hsu, N. C., Mulcahy, J. P., Sayer, A. M., and Sorooshian, A.: Uncertainty in aerosol-cloud radiative forcing is driven by clean conditions, Atmos. Chem. Phys., 23, 4115–4122, https://doi.org/10.5194/acp-23-4115-2023, 2023.

Guo, H., Campuzano-Jost, P., Nault, B. A., Day, D. A., Schroder, J. C., Kim, D., Dibb, J. E., Dollner, M., Weinzierl, B., and Jimenez, J. L.: The importance of size ranges in aerosol instrument intercomparisons: a case study for the Atmospheric Tomography Mission, Atmos. Meas. Tech., 14, 3631–3655, 2021.

Hodshire, A. L., Campuzano-Jost, P., Kodros, J. K., Croft, B., Nault, B. A., Schroder, J. C., Jimenez, J. L., and Pierce, J. R.: The potential role of methanesulfonic acid (MSA) in aerosol formation and growth and the associated radiative forcings, Atmos. Chem. Phys., 19, 3137–3160, 2019.

Hodzic, A., Campuzano-Jost, P., Bian, H., Chin, M., Colarco, P. R., Day, D. A., Froyd, K. D., Heinold, B., Jo, D. S., Katich, J. M., Kodros, J. K., Nault, B. A., Pierce, J. R., Ray, E., Schacht, J., Schill, G. P., Schroder, J. C., Schwarz, J. P., Sueper, D. T., Tegen, I., Tilmes, S., Tsigaridis, K., Yu, P., and Jimenez, J. L.: Characterization of organic aerosol across the global remote troposphere: a comparison of ATom measurements and global chemistry models, Atmos. Chem. Phys., 20, 4607–4635, 2020.

Hoffmann, E. H., Tilgner, A., Schrödner, R., Bräuer, P., Wolke, R. and Herrmann, H., An advanced modeling study on the impacts and atmospheric implications of multiphase dimethyl sulfide chemistry, Proc. Natl. Acad. Sci. USA, 113, 11776–11781, https://doi.org/10.1073/pnas.1606320113, 2016.

Holton, J. R., Haynes, P. H., McIntyre, M. E., Douglass, A. R., Rood, R. B., and Pfister, L.: Stratosphere-troposphere exchange, Rev. Geophys., 33, 403–439, https://doi.org/10.1029/95RG02097, 1995.

Hoesly, R. M., Smith, S. J., Feng, L., Klimont, Z., Janssens-Maenhout, G., Pitkanen, T., et al. (2018). Historical (1750–2014) anthropogenic emissions of reactive gases and aerosols from the Community Emissions Data System (CEDS). Geosci. Model Dev., 11, 369–408. https://doi.org/10.5194/gmd-11-369-2018.

Huang, R-J., Duan, J., Li, Y., Chen, Q., Chen, Y., Tang, M., Yang, L., Ni, H., Lin, C., Xu, W., Liu, Y., Chen, C., Yan, Z., Ovadnevaite, J., Ceburnis, D., Dusek, U., Cao, J., Hoffmann, T., & O'Dowd, C. D., Effects of NH3 and alkaline metals on the formation of particulate sulfate and nitrate in wintertime Beijing. Sci. Total Environ., 717, 137190, https://doi.org/10.1016/j.scitotenv.2020.137190, 2020.

Huey, L. G., Tanner, D. J., Slusher, D. L., Dibb, J. E., Arimoto, R., Chen, G., Davis, D., Buhr, M. P., Nowak, J. B., Mauldin III, R. L., Eisele, F. L., and Kosciuch, E.: CIMS measurements of HNO_3 and SO_2 at the South Pole during ISCAT 2000, Atmos. Environ., 38, 5411–5421, https://doi.org/10.1016/j.atmosenv.2004.04.037, 2004.

Ikeda, K., Tanimoto, H., Sugita, T., Akiyoshi, H., Kanaya, Y., Zhu, C., and Taketani, F.: Tagged tracer simulations of black carbon in the Arctic: transport, source contributions, and budget, Atmos. Chem. Phys., 17, 10515–10533, https://doi.org/10.5194/acp-17-10515-2017, 2017.

Jia, H., Ma, X., Yu, F., and Quaas, J.: Significant underestimation of radiative forcing by aerosol–cloud interactions derived from satellite-based methods, Nat. Commun., 12, https://doi.org/10.1038/s41467-021-23888-1, 2021.

Jia, H., Quaas, J., Gryspeerdt, E., Böhm, C., and Sourdeval, O.: Addressing the difficulties in quantifying the Twomey effect for marine warm clouds from multi-sensor satellite observations

and reanalysis, Atmos. Chem. Phys., 22, 7353–7372, https://doi.org/10.5194/acp-22-7353-2022, 2022.

Lin, X., Keppel-Aleks, G., Rogers, B. M., Birch, L.: Simulated CO2 tracer concentrations in the Northern Hemisphere from a tagged transport model GEOS-Chem v12.0.0 [Data set], University of Michigan - Deep Blue Data. https://doi.org/10.7302/rp59-rw53, 2020.

Moch, J. M., Mickley, L. J., Keller, C. A., Bian, H., Lundgren, E. W., Zhai, S., and Jacob, D. J.: Aerosol-radiation interactions in China in winter: Competing effects of reduced shortwave radiation and cloud-snowfall-albedo feedbacks under rapidly changing emissions, J. Geophys. Res. Atmos., 127, e2021JD035442, https://doi.org/10.1029/2021JD035442, 2022.
Myhre, G., B. H., Samset, M. Schulz, Y. Balkanski, S. Bauer, T. K. Berntsen, H. Bian, N. Bellouin, M. Chin, T. Diehl, R. C. Easter, J. Feichter, S. J. Ghan, D. Hauglustaine, T. Iversen, S. Kinne, A. Kirkevåg, J.-F. Lamarque, G. Lin, X. Liu, G. Luo, X. Ma, J. E. Penner, P. J. Rasch, Ø. Seland, R. B. Skeie, P. Stier, T. Takemura, K. Tsigaridis, Z. Wang, L. Xu, H. Yu, F. Yu, J.-H. Yoon, K. Zhang, H. Zhang, and C. Zhou, Radiative forcing of the direct aerosol effect from AeroCom Phase II simulations, Atmos. Chem. Phys., 13, 1853-1877, doi:10.5194/acp-13-1853-2013, 2013.

Josephson, D. C., Robinson, J. M., Chiotti, J,, Jirka, K. J., and Kraft, C. E.: Chemical and biological recovery from acid deposition within the Honnedaga Lake watershed, New York, USA, Environ. Monit. Assess., 186, 4391–4409, https://doi.org/10.1007/s10661-014-3706-9, 2014.

Jurkat, T., Kaufmann, S., Voigt, C., Schäuble, D., Jeßberger, P., and Ziereis, H.: The airborne mass spectrometer AIMS – Part 2: Measurements of trace gases with stratospheric or tropospheric origin in the UTLS, Atmos. Meas. Tech., 9, 1907–1923, https://doi.org/10.5194/amt-9-1907-2016, 2016.

Katich, J. M., Samset, B. H., Paul Bui, T., Dollner, M., Froyd, K. D., Campuzano-Jost, P., Nault, B. A., Schroder, J. C., Weinzierl, B., Schwarz J. P., Strong Contrast in Remote Black Carbon Aerosol Loadings Between the Atlantic and Pacific Basins, Journal of Geophysical Research: Atmospheres, Volume 123, Issue 23 p. 13,386-13,395, https://doi.org/10.1029/2018JD029206, 2018.

Kettle, A. J. and Andreae, M. O.: Flux of dimethylsulfide from the oceans: A comparison of updated data sets and flux models, J. Geophys. Res. Atmos., 105, 26793–26808, https://doi.org/10.1029/2000JD900252, 2000.

Klein, S. A., Zhang, Y., Zelinka, M. D., Pincus, R., Boyle, J., and Gleckler, P. J.: Are climate model simulations of clouds improving? An evaluation using the ISCCP simulator, J. Geophys. Res. Atmos., 118, 1329–1342, https://doi.org/10.1002/jgrd.50141, 2013.

Lana, A., Bell, T. G., Simó, R., Vallina, S. M., Ballabrera-Poy, J., Kettle, A. J., Dachs, J., Bopp, L., Saltzman, E. S., Stefels, J., Johnson, J. E., and Liss, P. S.: An updated climatology of surface

970   dimethlysulfide concentrations and emission fluxes in the global ocean, Global Biogeochem.
971   Cy., 25, GB1004, doi:10.1029/2010GB003850, 2011.

973   Liss, P.S., and Merlivat, L., Air-sea gas exchange rates: Introduction and synthesis, in The Role
974   of Air-Sea Gas Exchange in Geochemical Cycling, edited by P. Buat-Menard, pp. 113-127, D.
975   Reidel, Norwell, Mass., 1986.

977   Liu, M. and Matsui, H.: Improved simulations of global black carbon distributions by modifying
978   wet scavenging processes in convective and mixed-phase clouds, J. Geophys. Res. Atmos., 126,
979   e2020JD033890, https://doi.org/10.1029/2020JD033890, 2021.

981   Lund, M. T., Myhre, G., Haslerud, A. S., Skeie, R. B., Griesfeller, J., Platt, S. M., Kumar, R.,
982   Myhre, C. L., and Schulz, M.: Concentrations and radiative forcing of anthropogenic aerosols
983   from 1750 to 2014 simulated with the Oslo CTM3 and CEDS emission inventory, Geosci. Model
984   Dev., 11, 4909–4931, https://doi.org/10.5194/gmd-11-4909-2018, 2018.

986   Malavelle, F. F., Haywood, J. M., Jones, A., Gettelman, A., Clarisse, L., Bauduin, S., Allan, R.
987   P., Karset, I. H. H., Kristjánsson, J. E., Oreopoulos, L., Cho, N., Lee, D., Bellouin, N., Boucher,
988   O., Grosvenor, D. P., Carslaw, K. S., Dhomse, S., Mann, G. W., Schmidt, A., Coe, H., Hartley,
989   M. E., Dalvi, M., Hill, A. A., Johnson, B. T., Johnson, C. E., Knight, J. R., O'Connor, F. M.,
990   Partridge, D. G., Stier, P., Myhre, G., Platnick, S., Stephens, G. L., Takahashi, H., and
991   Thordarson, T.: Strong constraints on aerosol–cloud interactions from volcanic eruptions,
992   Nature, 546, 485-491, https://doi.org/10.1038/nature22974, 2017.

994   McDonnell, T. C., Driscoll, C. T., Sullivan, T. J., Burns, D. A., Baldigo, B. P., Shao, S., and
995   Lawrence, G. B.: Regional target loads of atmospheric nitrogen and sulfur deposition for the
996   protection of stream and watershed soil resources of the Adirondack Mountains, USA, Environ.
997   Pollut., 281, 117110, https://doi.org/10.1016/j.envpol.2021.117110, 2021.

999   Matsui, H.: Development of a global aerosol model using a two-dimensional sectional method: 1.
1000   Model design, J. Adv. Model. Earth Syst., 9, 1921–1947,
1001   https://doi.org/10.1002/2017MS000936, 2017.

1003   Matsui, H. and Mahowald, N.: Development of a global aerosol model using a two-dimensional
1004   sectional method: 2. Evaluation and sensitivity simulations, J. Adv. Model. Earth Syst., 9, 1887–
1005   1920, https://doi.org/10.1002/2017MS000937, 2017.

1007   Molod, A.: Constraints on the Total Water PDF in GCMs from AIRS and a High Resolution
1008   Model, J. Climate, 25, 8341–8352, https://doi.org/10.1175/JCLI-D-11-00412.1, 2012.

1010   Moorthi, S. and Suarez, M. J.: Relaxed Arakawa-Schubert. A parameterization of moist
1011   convection for general circulation models, Mon. Weather Rev., 120, 978–1002,
1012   https://doi.org/10.1175/1520-0493(1992)120<0978:RASAPO>2.0.CO;2, 1992.

1014   Myhre, G., Samset, B. H., Schulz, M., Balkanski, Y., Bauer, S., Berntsen, T. K., Bian, H.,
1015   Bellouin, N., Chin, M., Diehl, T., Easter, R. C., Feichter, J., Ghan, S. J., Hauglustaine, D.,

Iversen, T., Kinne, S., Kirkevåg, A., Lamarque, J.-F., Lin, G., Liu, X., Lund, M. T., Luo, G., Ma, X., van Noije, T., Penner, J. E., Rasch, P. J., Ruiz, A., Seland, Ø., Skeie, R. B., Stier, P., Takemura, T., Tsigaridis, K., Wang, P., Wang, Z., Xu, L., Yu, H., Yu, F., Yoon, J.-H, Zhang, K., Zhang, H., and Zhou, C.: Radiative forcing of the direct aerosol effect from AeroCom Phase II simulations, Atmos. Chem. Phys., 13, 1853–1877, https://doi.org/10.5194/acp-13-1853-2013, 2013.

Nicely, J. M., Duncan, B. N., Hanisco, T. F., Wolfe, G. M., Salawitch, R. J., Deushi, M., Haslerud, A. S., Jöckel, P., Josse, B., Kinnison, D. E., Klekociuk, A., Manyin, M. E., Marécal, V., Morgenstern, O., Murray, L. T., Myhre, G., Oman, L. D., Pitari, G., Pozzer, A., Quaglia, I., Revell, L. E., Rozanov, E., Stenke, A., Stone, K., Strahan, S., Tilmes, S., Tost, H., Westervelt, D. M., and Zeng, G.: A machine learning examination of hydroxyl radical differences among model simulations for CCMI-1, Atmos. Chem. Phys., 20, 1341–1361, https://doi.org/10.5194/acp-20-1341-2020, 2020.

Nielsen, J. E., Pawson, S., Molod, A., Auer, B., da Silva, A. M., Douglass, A. R., Wargan, K.: Chemical mechanisms and their applications in the Goddard Earth Observing System (GEOS) earth system model. J. Adv. Model. Earth Sys., 9, 3019–3044. https://doi.org/10.1002/2017MS001011, 2017.

Nightingale P. D., Malin G., Law C. S., Watson A. J., Liss P. S., Liddicoat M. I., et al. In situ evaluation of air-sea gas exchange parameterizations using novel conservative and volatile tracers. Global Biogeochem. Cy. 14, 373–387, https://doi.org/10.1029/1999gb900091, 2000.

Penner, A., Prather, J. E., Ramanathan, K. A., Ramaswamy, V., Rasch, V., Ravishankara, P. J., Rosenfeld, A. R., Stephens, D., and Wood, R.: Improving our fundamental understanding of the role of aerosol–cloud interactions in the climate system, P. Natl. Acad. Sci. USA, 113, 5781–5790, https://doi.org/10.1073/pnas.1514043113, 2016.

Rasch, P. J., Xie, S., Ma, P. -L., Lin, W., Wang, H., Tang, Q., Burrows, S. M., Caldwell, P., Zhang, K., Easter, R. C., Cameron-Smith, P., Singh, B., Wan, H., Golaz, J.-C., Harrop, B. E., Roesler, E., Bacmeister, J., Larson, V. E., Evans, K. J., Qian, Y., Taylor, M., Leung, L. R., Zhang, Y., Brent, L., Branstetter, M., Hannay, C., Mahajan, S., Mametjanov, A., Neale, R., Richter, J. H., Yoon, J.-H., Zender, C. S., Bader, D., Flanner, M., Foucar, J. G., Jacob, R., Keen, N., Klein, S. A., Liu, X., Salinger, A. G., Shrivastava, M., and Yang, Y.: An Overview of the Atmospheric Component of the Energy Exascale Earth System Model, J. Adv. Model. Earth Syst., 11, 2377–2411, https://doi.org/10.1029/2019MS001629, 2019.

Rickly, P. S., Xu, L., Crounse, J. D., Wennberg, P. O., and Rollins, A. W.: Improvements to a laser-induced fluorescence instrument for measuring SO_2 – impact on accuracy and precision, Atmos. Meas. Tech., 14, 2429–2439, https://doi.org/10.5194/amt-14-2429-2021, 2021.

Rienecker, M., Suarez, M., Todling, R., Bacmeister, J., Takacs, L., Liu, H.-C., Gu, W., Sienkiewicz, M., Koster, R., Gelaro, R., Stajner, I., and Nielsen, J.: The GEOS-5 Data Assimilation System – Documentation of Versions 5.0.1, 5.1.0, and 5.2.0., Vol. 27 of Technical

Report Series on Global Modeling and Data Assimilation, NASA Goddard Space Flight Center, Greenbelt, MD, USA, 2008.

Rissman, T. A., Nenes, A., and Seinfeld, J. H.: Chemical amplification (or dampening) of the Twomey effect: Conditions derived from droplet activation theory, J. Atmos. Sci., 61(8), 919–930, https://doi.org/10.1175/1520-0469(2004)061<0919:CAODOT>2.0.CO;2, 2004.

Rollins, A. W., Thornberry, T. D., Ciciora, S. J., McLaughlin, R. J., Watts, L. A., Hanisco, T. F., Baumann, E., Giorgetta, F. R., Bui, T. V., Fahey, D. W., and Gao, R.-S.: A laser-induced fluorescence instrument for aircraft measurements of sulfur dioxide in the upper troposphere and lower stratosphere, Atmos. Meas. Tech., 9, 4601–4613, https://doi.org/10.5194/amt-9-4601-2016, 2016.

Saltzman, E. S., King, D. B., Holmen, K., and Leck, C., Experimental Determination of the Diffusion Coefficient of Dimethylsulfide in Water, J. of Geophys. Res. Atoms., Vol. 98, No. C9, 16,481-16,486, 1993.

Schill, G. P., Froyd, K. D., Bian, H., Kupc, A., Williamson, C., Brock, C. B., Ray, E., Hornbrook, R. S., Hills, A. J., Apel, E. C., Chen, M., Colarco, P., and Murphy, D. M., The ubiquity of dilute, aged smoke in the global remote troposphere and its effect on climate, Nature Geoscience, 13(6), https://doi:10.1038/s41561-020-0586-1, Jun., 2020.

Schueneman, M. K., Nault, B. A., Campuzano-Jost, P., Jo, D. S., Day, D. A., Schroder, J. C., Palm, B. B., Hodzic, A., Dibb, J. E., and Jimenez, J. L.: Aerosol pH indicator and organosulfate detectability from aerosol mass spectrometry measurements, Atmos. Meas. Tech., 14, 2237–2260, 2021.

Seinfeld, J. H., Bretherton, C., Carslaw, K. S., Coe, H., DeMott, P. J., Dunlea, E. J., Feingold, G., Ghan, S., Guenther, A. B., Kahn, R., Kraucunas, I., Kreidenweis, S. M., Molina, M. J., Nenes, A., Penner, J. E., Prather, K. A., Ramanathan, V., Ramaswamy, V., Rasch, P. J., Ravishankara, A. R., Rosenfeld, D., Stephens, G., and Wood, R.: Improving our fundamental understanding of the role of aerosol–cloud interactions in the climate system, P. Natl. Acad. Sci. USA, 113, 5781–5790, https://doi.org/10.1073/pnas.151404311, 2016.

Schulz, M., Textor, C., Kinne, S., Balkanski, Y., Bauer, S., Berntsen, T., Berglen, T., Boucher, O., Dentener, F., Guibert, S., Isaksen, I. S. A., Iversen, T., Koch, D., Kirkevåg, A., Liu, X., Montanaro, V., Myhre, G., Penner, J. E., Pitari, G., Reddy, S., Seland, Ø., Stier, P., and Takemura, T.: Radiative forcing by aerosols as derived from the AeroCom present-day and pre-industrial simulations, Atmos. Chem. Phys., 6, 5225–5246, https://doi.org/10.5194/acp-6-5225-2006, 2006

Simpson, I. J., Colman, J. J., Swanson, A. L., Bandy, A. R., Thornton, D. C., Blake, D. R., and F. S. Rowland, F. S.: Aircraft Measurements of Dimethyl Sulfide (DMS) Using a Whole Air Sampling Technique, J. Atmos. Chem., 39, 191-213, https://doi.org/10.1023/A:1010608529779, 2001.

1107 Slingo, J.: The development and verification of a cloud prediction scheme for the ECMWF
1108 model, Q. J. Roy. Meteor. Soc., 113, 899–927, https://doi.org/10.1002/qj.49711347710, 1987.
1109
1110 Smith, R. N. B.: A scheme for predicting layer clouds and their water content in a general
1111 circulation model, Q. J. Roy. Meteor. Soc., 116, 435–460,
1112 https://doi.org/10.1002/qj.49711649210, 1990.
1113
1114 Søvde, O. A., Prather, M. J., Isaksen, I. S. A., Berntsen, T. K., Stordal, F., Zhu, X., Holmes, C.
1115 D., and Hsu, J.: The chemical transport model Oslo CTM3, Geosci. Model Dev., 5, 1441–1469,
1116 https://doi.org/10.5194/gmd-5-1441-2012, 2012.
1117
1118 Strode, S. A., Liu, J., Lait, L., Commane, R., Daube, B., Wofsy, S., Conaty, A., Newman, P., and
1119 Prather, M.: Forecasting carbon monoxide on a global scale for the ATom-1 aircraft mission:
1120 insights from airborne and satellite observations and modeling, Atmos. Chem. Phys., 18, 10955–
1121 10971, https://doi.org/10.5194/acp-18-10955-2018, 2018.
1122
1123 Tan, J., Fu, J. S., Dentener, F., Sun, J., Emmons, L., Tilmes, S., Flemming, J., Takemura, T.,
1124 Bian, H., Zhu, Q., Yang, C.-E., and Keating, T.: Source contributions to sulfur and nitrogen
1125 deposition – an HTAP II multi-model study on hemispheric transport, Atmos. Chem. Phys., 18,
1126 12223–12240, https://doi.org/10.5194/acp-18-12223-2018, 2018.
1127
1128 Thompson, C. R., Wofsy, S. C., Prather, M. J., Newman, P. A., Hanisco, T. F., Ryerson, T. B.,
1129 Fahey, D. W., Apel, E. C., Brock, C. A., Brune, W. H., Froyd, K., Katich, J. M., Nicely, J. M.,
1130 Peischl, J., Ray, E., Veres, P. R., Wang, S., Allen, H. M., Asher, E., Bian, H., Blake, D.,
1131 Bourgeois, I., Budney, J., Paul Bui, T., Butler, A., Campuzano-Jost, P., Chang, C., Chin, M.,
1132 Commane, R., Correa, G., Crounse, J. D., Daube, B., Dibb, J. E., Digangi, J. P., Diskin, G. S.,
1133 Dollner, M., Elkins, J. W., Fiore, A. M., Flynn, C. M., Guo, H., Hall, S. R., Hannun, R. A., Hills,
1134 A., Hintsa, E. J., Hodzic, A., Hornbrook, R. S., Greg Huey, L., Jimenez, J. L., Keeling, R. F.,
1135 Kim, M. J., Kupc, A., Lacey, F., Lait, L. R., Lamarque, J.-F., Liu, J., Mckain, K., Meinardi, S.,
1136 Miller, D. O., Montzka, S. A., Moore, F. L., Morgan, E. J., Murphy, D. M., Murray, L. T., Nault,
1137 B. A., Andrew Neuman, J., Nguyen, L., Gonzalez, Y., Rollins, A., Rosenlof, K., Sargent, M.,
1138 Schill, G., Schwarz, J. P., St. Clair, J. M., Steenrod, S. D., Stephens, B. B., Strahan, S. E., Strode,
1139 S. A., Sweeney, C., Thames, A. B., Ullmann, K., Wagner, N., Weber, R., Weinzierl, B.,
1140 Wennberg, P. O., Williamson, C. J., Wolfe, G. M., and Zeng, L.: THE NASA ATMOSPHERIC
1141 TOMOGRAPHY (ATom) MISSION: Imaging the Chemistry of the Global Atmosphere, Bull.
1142 Am. Meteorol. Soc., 103, E761-E790, https://doi.org/10.1175/BAMS-D-20-0315.1, 2022.
1143
1144 Tiedtke, M.: Representation of clouds in large-scale models, Mon. Weather Rev., 121, 3040–
1145 3061, https://doi.org/10.1175/1520-0493(1993)121<3040:ROCILS>2.0.CO;2, 1993.
1146
1147 Wang, H., Easter, R. C., Zhang, R., Ma, P., Singh, B., Zhang, K., Ganguly, D., Rasch, P. J.,
1148 Burrows, S. M., Ghan, S. J., Lou, S., Qian, Y., Yang, Y., Feng, Y., Flanner, M., Leung, L. R.,
1149 Liu, X., Shrivastava, M., Sun, J., Tang, Q., Xie, S., and Yoon, J.: Aerosols in the E3SM Version
1150 1: New Developments and Their Impacts on Radiative Forcing, J. Adv. Model. Earth Syst., 12,
1151 e2019MS001851, https://doi.org/10.1029/2019MS001851, 2020.
1152

Wang, D., Zhu, B., Wang, H., and Sun, L., Simulation study on the indirect effect of sulfate on the summer climate over the eastern China monsoon region, Sci. Rep., 11, 8295, https://doi.org/10.1038/s41598-021-87832-5, 2021.

Williamson, C. J., Kupc, A., Axisa, D., Bilsback, K. R, Bui, T. P., Campuzano-Jost, P., Dollner, M., Froyd, K. D., Hodshire, A. L., Jimenez, J. L., Kodros, J. K., Luo, G., Murphy, D. M., Nault, B. A., Ray, E. A., Weinzierl, B., Wilson, J. C., Yu, F., Yu, P., Pierce, J. R., and Brock, C. A.: A large source of cloud condensation nuclei from new particle formation in the tropics, Nature, 574, 399–403, https://doi.org/10.1038/s41586-019-1638-9, 2019.

Yan, J., Jung, J., Zhang, M., Xu, S., Lin, Q., Zhao, S., and Chen, L.: Significant Underestimation of Gaseous Methanesulfonic Acid (MSA) over Southern Ocean, Environ. Sci. Technol., 53 (22), pp. 13064-13070, https://doi.org/10.1021/acs.est.9b05362, 2019.

Yu, P. F., Froyd, K. D., Portmann, R.W., Toon, O. B., Freitas, S. R., Bardeen, C. G., Brock, C., Fan, T. Y., Gao, R. S., Katich, J. M., Kupc, A., Liu, S., Maloney, C., Murphy, D. M., Rosenlof, K. H., Schill, G., Schwarz, J. P., and Williamson, C.: Efficient In-Cloud Removal of Aerosols by Deep Convection, Geophys. Res. Lett., 46, 1061–1069, https://doi.org/10.1029/2018gl080544, 2019.

Zhang, K., Zhang, W., Wan, H., Rasch, P. J., Ghan, S. J., Easter, R. C., Shi, X., Wang, Y., Wang, H., Ma, P.-L., Zhang, S., Sun, J., Burrows, S. M., Shrivastava, M., Singh, B., Qian, Y., Liu, X., Golaz, J.-C., Tang, Q., Zheng, X., Xie, S., Lin, W., Feng, Y., Wang, M., Yoon, J.-H., and Leung, L. R.: Effective radiative forcing of anthropogenic aerosols in E3SM version 1: historical changes, causality, decomposition, and parameterization sensitivities, Atmos. Chem. Phys., 22, 9129–9160, https://doi.org/10.5194/acp-22-9129-2022, 2022.

Zhu, J., Penner, J. E., Lin, G., Zhou, C., Xu, L., and Zhuang, B.: Mechanism of SOA formation determines magnitude of radiative effects. Proceedings of the National Academy of Sciences of the United States of America, 114, 12685–12690, https://doi.org/10.1073/pnas.1712273114, 2017.

Zhu, J., Penner, J. E., Yu, F., Sillman, S., Andreae, M. O., and Coe, H.: Decrease in radiative forcing by organic aerosol nucleation, climate, and land use change. Nature Commun, , 10, 423, https://doi.org/10.1038/s41467-019-08407-7, 2019.

1200   Table 1. ATom sulfur measurements used in the study

Instrument	SO4		SO2		MSA		DMS	
	AMS[a]	PALMS[b]	CIMS[c]	LIF[d]	AMS	PALMS	TOGA[e]	WAS[f]
ATom deployment(s)	1 to 4	1 to 4	1 to 4	4	1 to 4	1 to 4	2 to 4	1 to 4
Frequency	60 s	180 s	1 s	1 s	1 s	180 s	120 s	Variable but ~180 s
Accuracy	±35% (2s)	±60% at 10 ng m-3 ±20% at 1 µg m-3	±25%	± 9% (1s)	±35% (2s)	±70%	15% or better	15%
precision			130pptv					10%
Detection limit	5-15 ng sm-3	~10 ng sm-3		2 pptv	2.5 ng sm-3 (60 s)	~15 ng sm-3	1 ppt	1 ppt
Cut-off size (dry diameter)	~0.75 µm	0.1-3 µm			~0.75 µm	0.1-3 µm		
Primary Investigator(s)	Jose Jimenez and Pedro Campuzano Jost	Karl Froyd and Gregory Schill	Paul Wennberg	Andrew Rollins	Jose Jimenez and Pedro Campuzano Jost	Karl Froyd and Gregory Schill	Eric Apel	Donald Blake
References	Guo et al., 2021; Schueneman et al., 2021	Froyd et al., 2019	Allen et al., 2022; Crounse et al., 2006	Rollins et al., 2016	Hodshire et al., 2019	Froyd et al., 2019	Apel et al., 2015	Simpson et al., 2001

1201   [a]AMS: Aerosol Mass Spectrometer
1202   [b]PALMS: Particle Analysis by Laser Mass Spectrometry
1203   [c]CIMS: Chemical Ionization Mass Spectrometer
1204   [d]LIF: Laser Induced Fluorescence
1205   [e]TOGA: NCAR Trace Organic Gas Analyzer
1206   [f]WAS: Whole Air Sampler

1207
1208   Table 2. AeroCom Models used in this study

Model Abbreviation	Model Version	Nominal Resolution	Vertical Levels	Meteorological Fields	Ocean Surface Temperature Data	Interactive Aerosol-Meteorology	Endogenous Oxidants	Endogeous DMS Emission	Aerosol Module	Anthropogenic Emission	Volcano Emission	Key References
CAM-ATRAS	CAM5-ATRAS2	1.9° × 2.5°	30	MERRA-2	HadSST	Yes	Yes	No	Microphysics, 12 sectional size bins, and internal mixing of aerosol constituents in each bin.	CEDS (Hoesly et al., 2018),	Degassing (Andres and Kasgnoc, 1998), Eruption (Neely and Schmidt, 2016)	Liu and Matsui 2021; Matsui 2017; Matsui and Mahowald, 2017
E3SM	v1.0	1° × 1°	72	ERA-Interim	HadSST	Yes	No	No	Microphysics, MAM4, internal mixing within a mode, external mixing between modes	CEDS (Hoesly et al., 2018)	Contineous emission (Denener et al., 2006). No eruptive emissions.	Rasch et al., 2019; Wang et al., 2020; Zhang et al. 2022
GEOS	Icarus-3_3_p2	1° × 1°	72	MERRA-2	MERRA sst	Yes	No	Yes	GOCART, Bulk, external mixing	CEDS (Hoesly et al., 2018)	Carns et al., 2016, 2017	Bian 2017; Colarco et al., 2010; Chin et al., 2000
IMPACT		1.9° × 2.5°	30	Open IFS ECMWF	HadSST	No	Yes	no	Microphysics, internal mixing within a mode, external mixing between modes	CEDS (Hoesly et al., 2018)	AeroCom volcanic emissions	Zhu et al., 2017; Zhu et al., 2019
OsloCTM3	OsloCTM3v1.02	2.25° × 2.25°	60	Open IFS ECMWF	Open IFS ECMWF	No	Yes	Yes	Bulk, external mixing	SSP245 with linear interpolation for 2017	AeroCom volcanic emissions, continuous from Dentener (2006)	Lund et al., 018; Søvde et al., 2012

1209
1210   Table 3. DMS emission used/calcuated by the five AeroCom models

Model abbreviation	Emission inventory	DMS concentration in sea water	DMS flux calculation	Meteorological fields
CAM-ATRAS	No	Lana et al. (2011)	Nightingale et al. 2000	Wind from ECMWF-IFS
E3SM	Yes			
GEOS	No	Lana et al. (2011)	Liss and Merlivat, (1986), Saltzman et al. (1993)	SST and wind from GEOS
IMPACT	Yes			
OsloCTM3	No	Kettle and Andreae (2000)	Nightingale et al. (2000)	Wind from ECMWF-IFS

1211
1212 Table 4. Global sulfur budget in 2017

		Emission	SUPSO$_2$[1]	SUPMSA	SUPSO$_4$	Dry	Wet	TotalSource	Burden	Lifetime
		TgS/yr	TgS/yr	TgS/yr	TgS/yr	TgS/yr	TgS/yr	TgS/yr	TgS	days
CAM-ATRAS	DMS	26.05	-26.05	--	--	--	--	26.05	0.13	1.8
	SO2	68.67	26.05	--	-55.67	-39.05		94.72	0.445	1.7
	SO4	1.76	--	--	55.67	-4.72	-53.23	58.09	0.67	4.2
E3SM	DMS	19.43	-19.40	--	--	--	--	19.43	0.0658	1.24
	SO2	67.92	19.40	--	-38.56	-48.76		87.32	0.3825	1.60
	SO4	1.74	--	--	38.56	-6.95	-33.31	40.31	0.6183	5.60
GEOS	DMS	15.57	-14.84	-0.74	--	--	--	15.57	0.0252	0.59
	SO2	67.06	14.84		-37.49	-32.93	-11.39	81.90	0.3488	1.55
	SO4	1.68	--	--	37.49	-5.27	-33.90	39.17	0.3269	3.05
	MSA	--	--	0.74	--	-0.10	-0.64	-.74	0.0063	3.11
IMPACT	DMS	18.22	-18.22	--	--	--	--	18.05	0.0369	0.75
	SO2	64.76	18.22	--	-51.44	-31.29	--	82.98	0.4134	1.82
	SO4	1.36	--	--	51.44	-3.48	-49.32	52.80	0.7502	5.19
OsloCTM3	DMS	26.93	-26.93	--	--	--	--	26.93	0.1496	2.03
	SO2	52.80	26.93	--	-49.23	-29.01	-1.49	79.73	0.2346	1.08
	SO4	1.053	--	--	55.49	-6.35	-50.29	56.54	0.8681	5.60

1213 [1]SUPSO$_2$: chemical production for SO$_2$
1214
1215
1216 Table 5. Global and annual sulfate multimodel mean and diversity from three AeroCom phases

	AeroCom-I	AeroCom-II		AeroCom-III	
reference	Textor et al., 2006	Myher et al., 2013	Kipling et al., 2016	Gliß et al., 2021	This work
Study year	2000	2006	2006	2010	2017
# of models	16	16	18	14	5
MMM (Tg)	2.0	1.05	1.48	1.87	1.94
δ (%)	25.0	26.4	34.6	38.8	28.0
observation	No	No	No	AC, AS, AE, and AOD from Ground station and AOD from MODIS	DMS, SO$_2$, SO$_4$ and MSA from ATom

1217
1218
1219
1220
1221
1222
1223
1224
1225
1226
1227
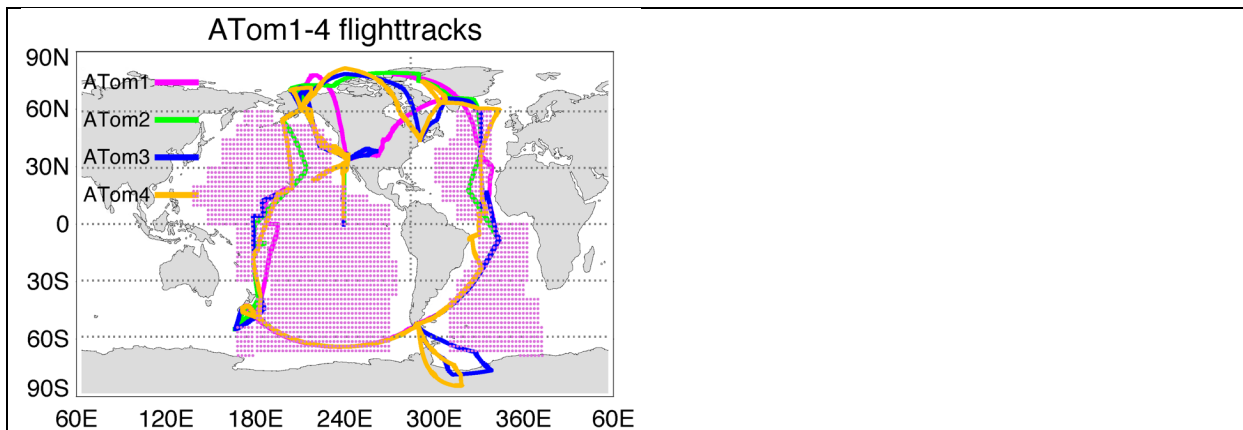
Figure 1. Flight tracks of ATom-1 to -4 and regions for the analysis of SO4 source origins (shaded area). Periods of the four ATom deployments are ATom-1 (July-August 2016), ATom-2 (January-February 2017), ATom-3 (September-October 2017) and ATom-4 (April-May 2018).

1228
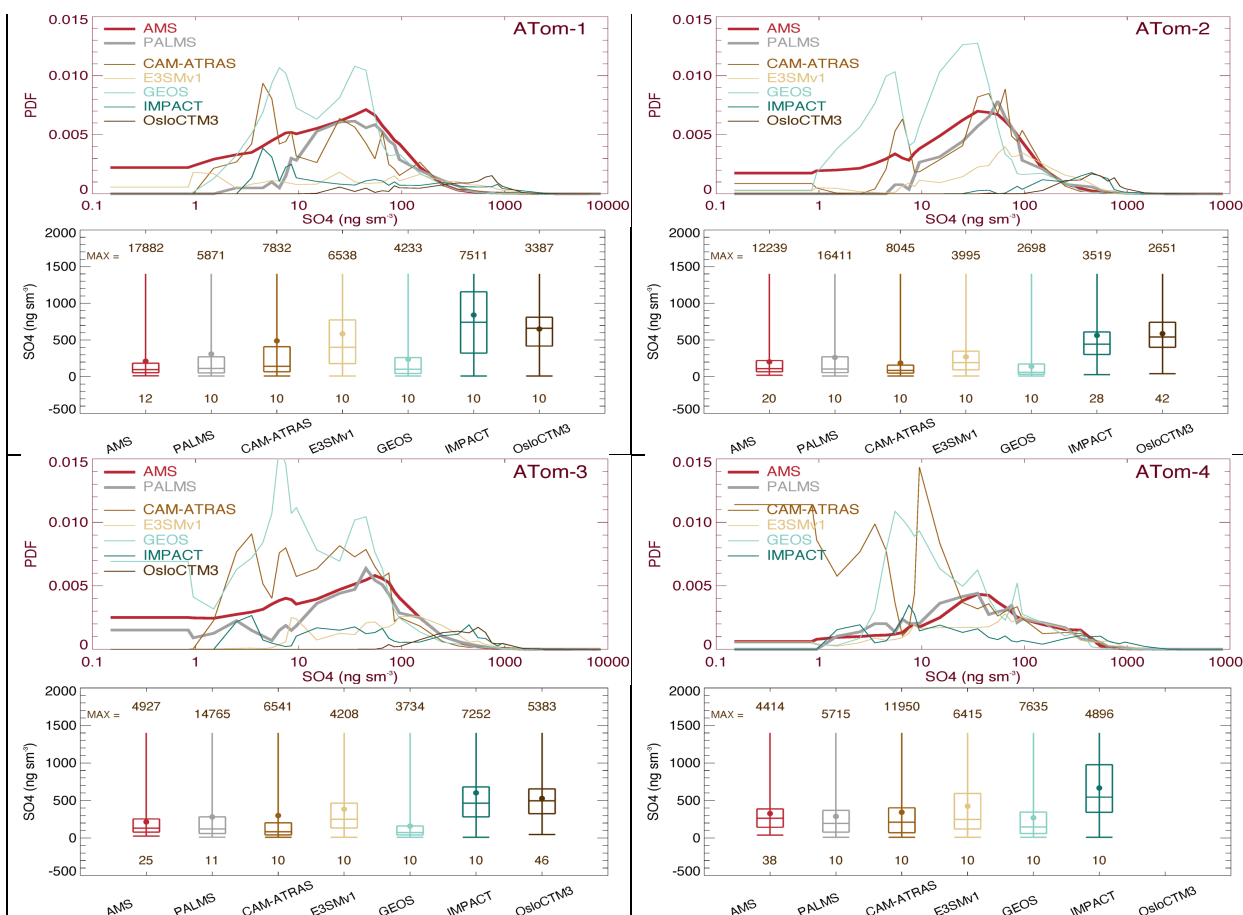
Figure 2. SO4 probability density functions (PDF) and its statistical values shown by box-and-whisker for the four ATom deployments. All data (AMS in red, PALMS in grey, and five model simulations in other colors) are sampled at 10-s points. Statistical values include the range of the data from minimum to maximum, the three levels of the 25th, 50th (median), and 75th percentiles in the box, and the filled circle for the mean. Statistical values are calculated when measured values are above the detection limit (DL).

1229
1230

Figure 3. Similar to Fig. 2 but for SO₂. Observational data are CIMS (red) for ATom-1 to -4 and LIF (grey) for ATom-4 from ATom 10-s merged data. PDFs and statistical values are calculated at points where CIMS (and LIF in ATom-4) measured SO₂ are above DL (e.g., 2 pptv).
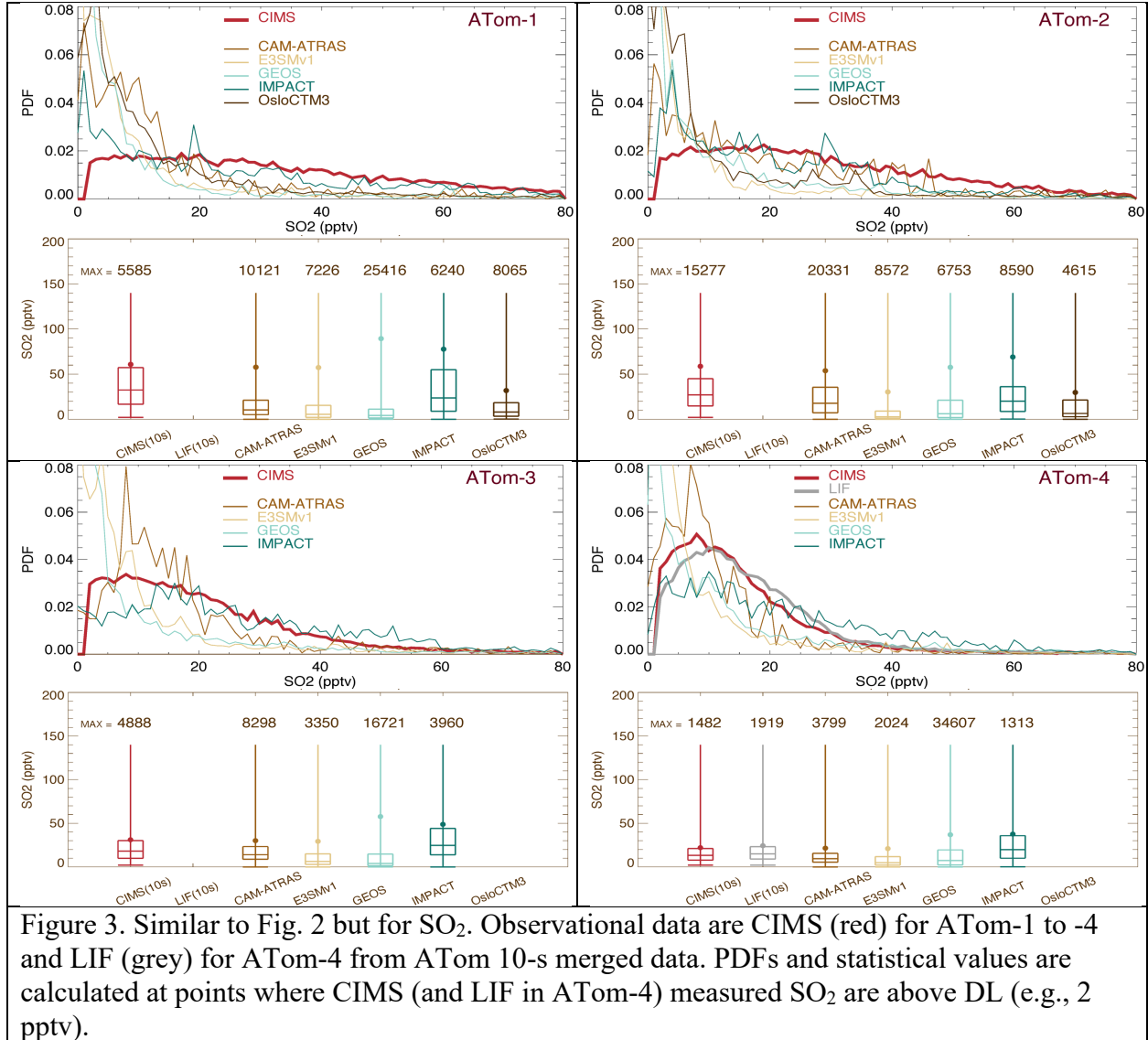
1231
1232
1233
1234
1235
1236
1237
1238
1239
1240
1241
1242
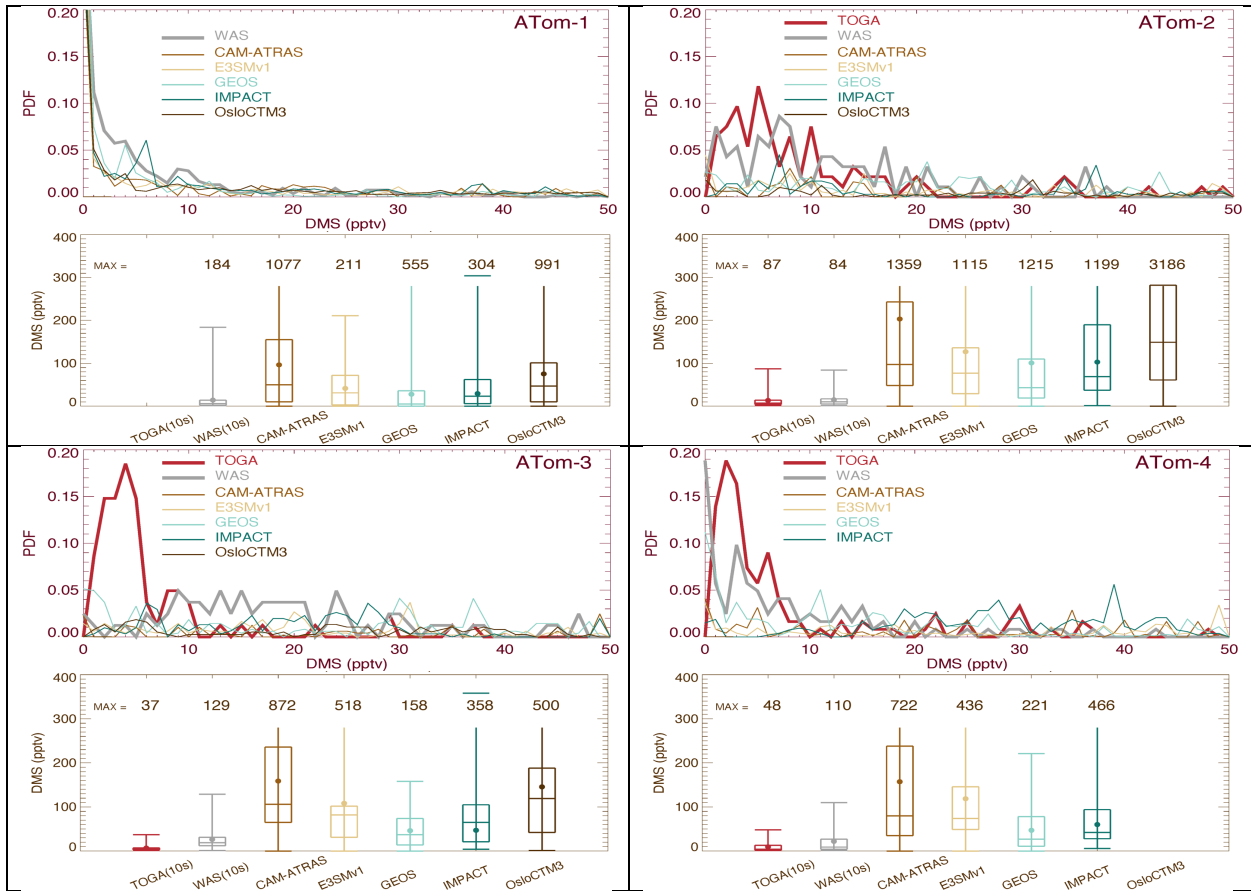
Figure 4. Similar to Fig. 2 but for DMS for ATom-1 to -4. The original data reported by TOGA (e.g., 35-s) and by WAS (e.g., ~60-s) have also been converted to 10-s frequency. Data included in PDF and statistical analysis are on 10-s points where DMS measured by both TOGA and WAS are above DL (i.e., 1 pptv).

1243
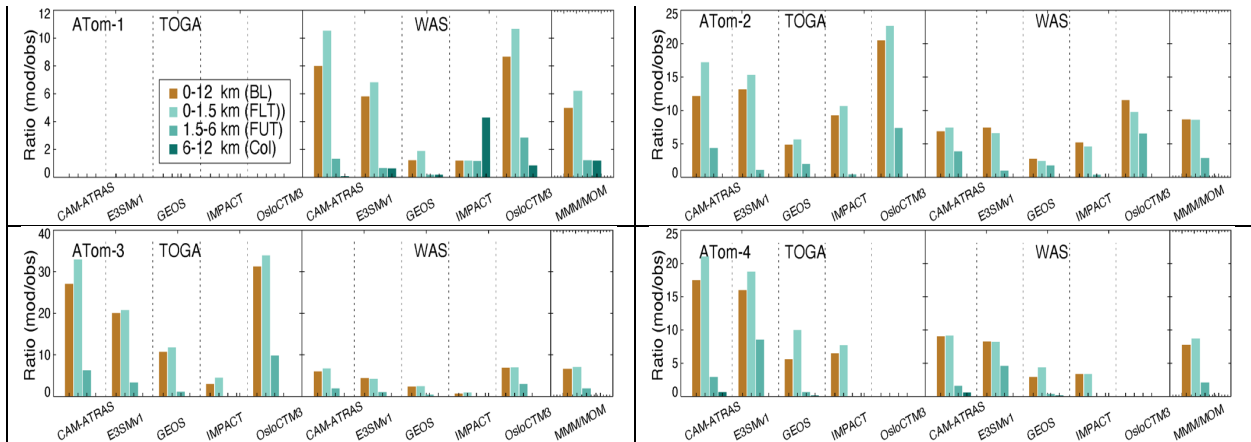
Figure 5. Ratio of DMS median values between model simulation and observation for four ATom deployments. Ratio analyses are performed on four vertical ranges as shown in four colors (see legend in ATom-1). The last column "MMM/MOM" refers to multi-model median to multi-observation median.
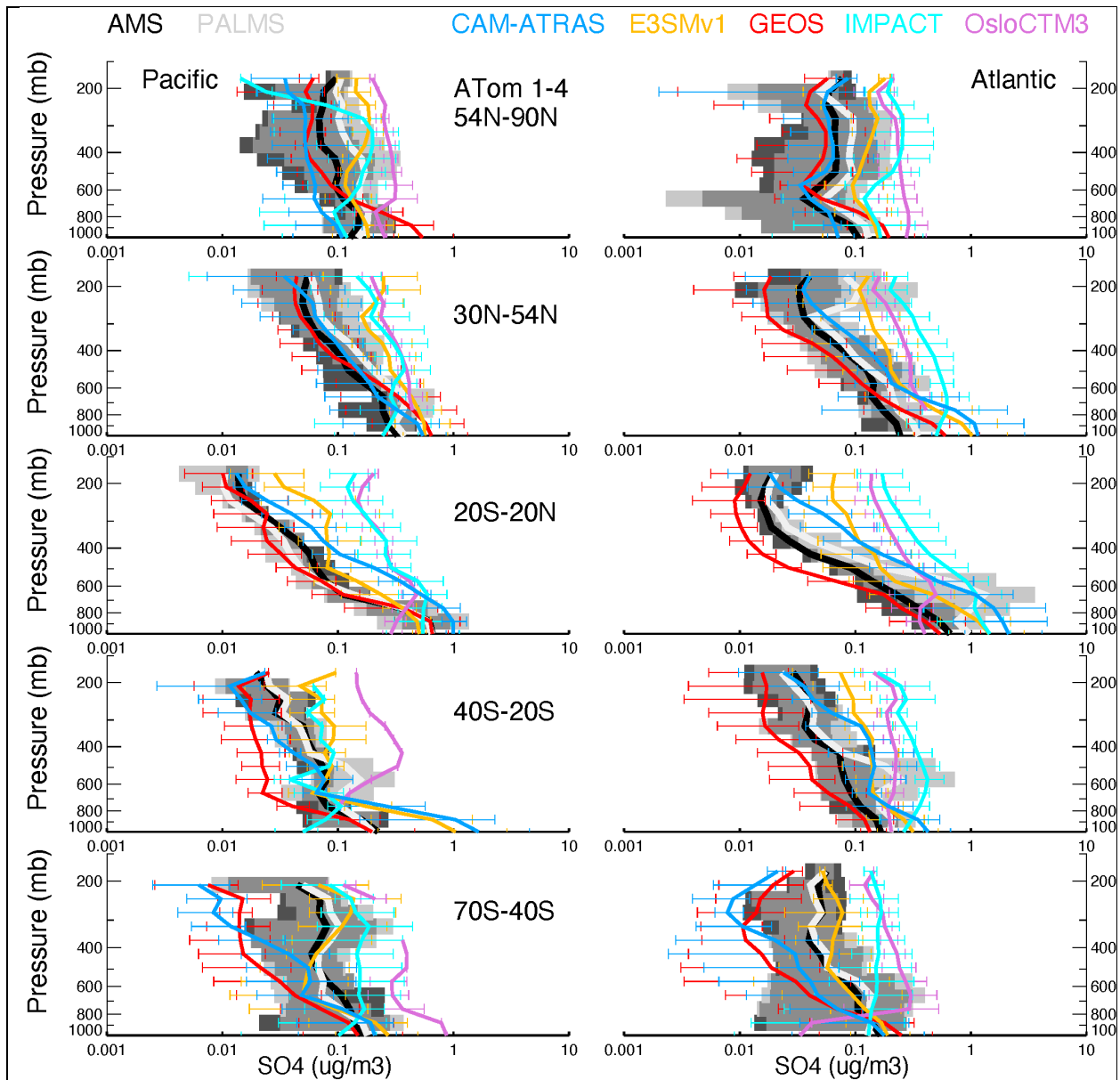
Figure 6. Observed and modeled vertical profiles of SO$_4$ in 1-km vertical bins averaged for four ATom deployments (lines) and variation across the four AToms (shaded area for measurements and horizontal bars for simulations). ATom measurements are shown in black (AMS) and light grey (PALMS) while model results are shown in other colors. Comparisons are conducted only when both observational measurements above detect limitation are available. Comparisons are separated into five latitude bands from the Northern to the Southern Hemisphere, and into Pacific and Atlantic Basins.

1244
1245
1246
1247
1248
1249
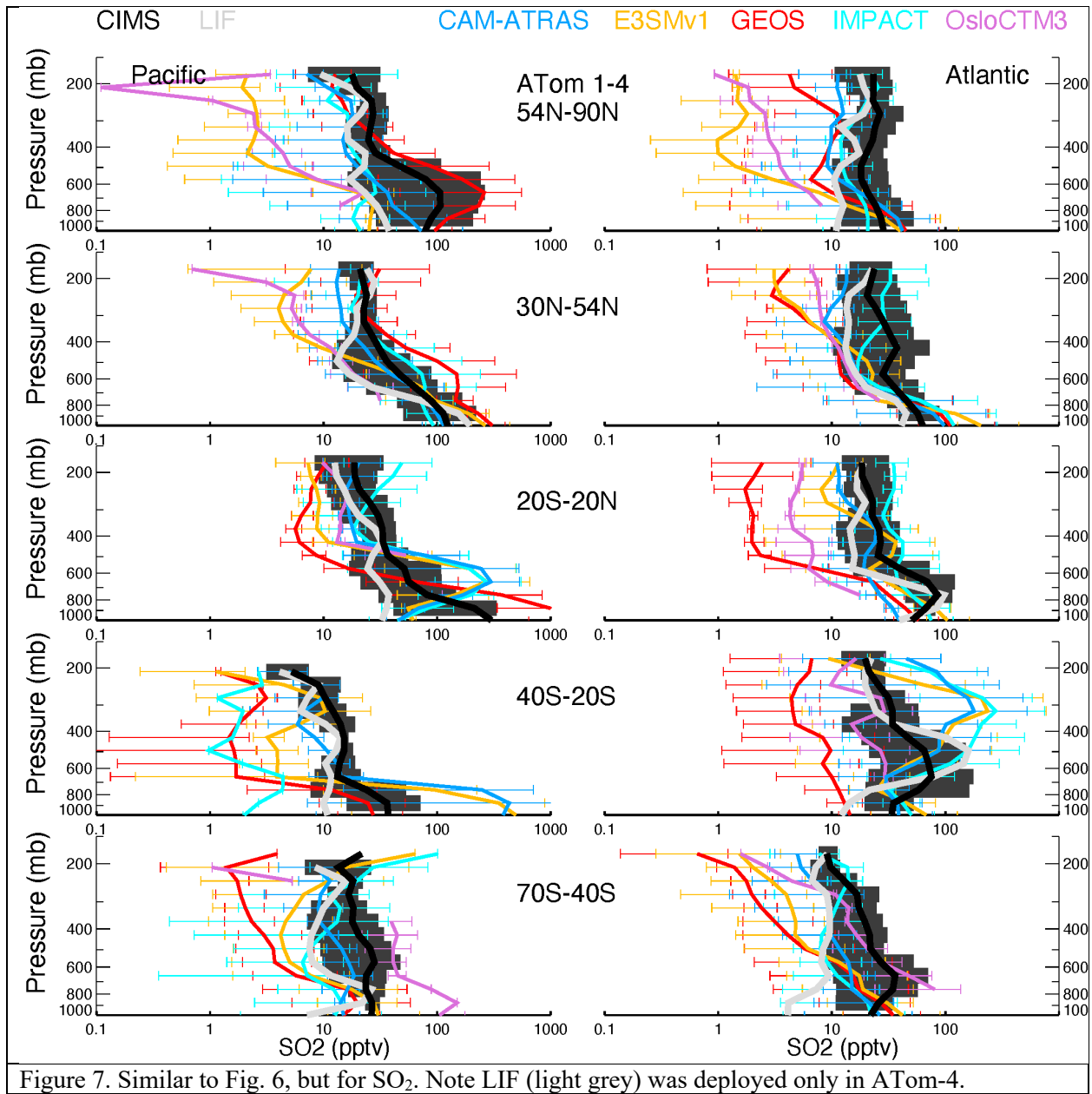
Figure 7. Similar to Fig. 6, but for SO₂. Note LIF (light grey) was deployed only in ATom-4.

1250
1251
1252
1253
1254
1255
1256
1257
1258
1259
1260
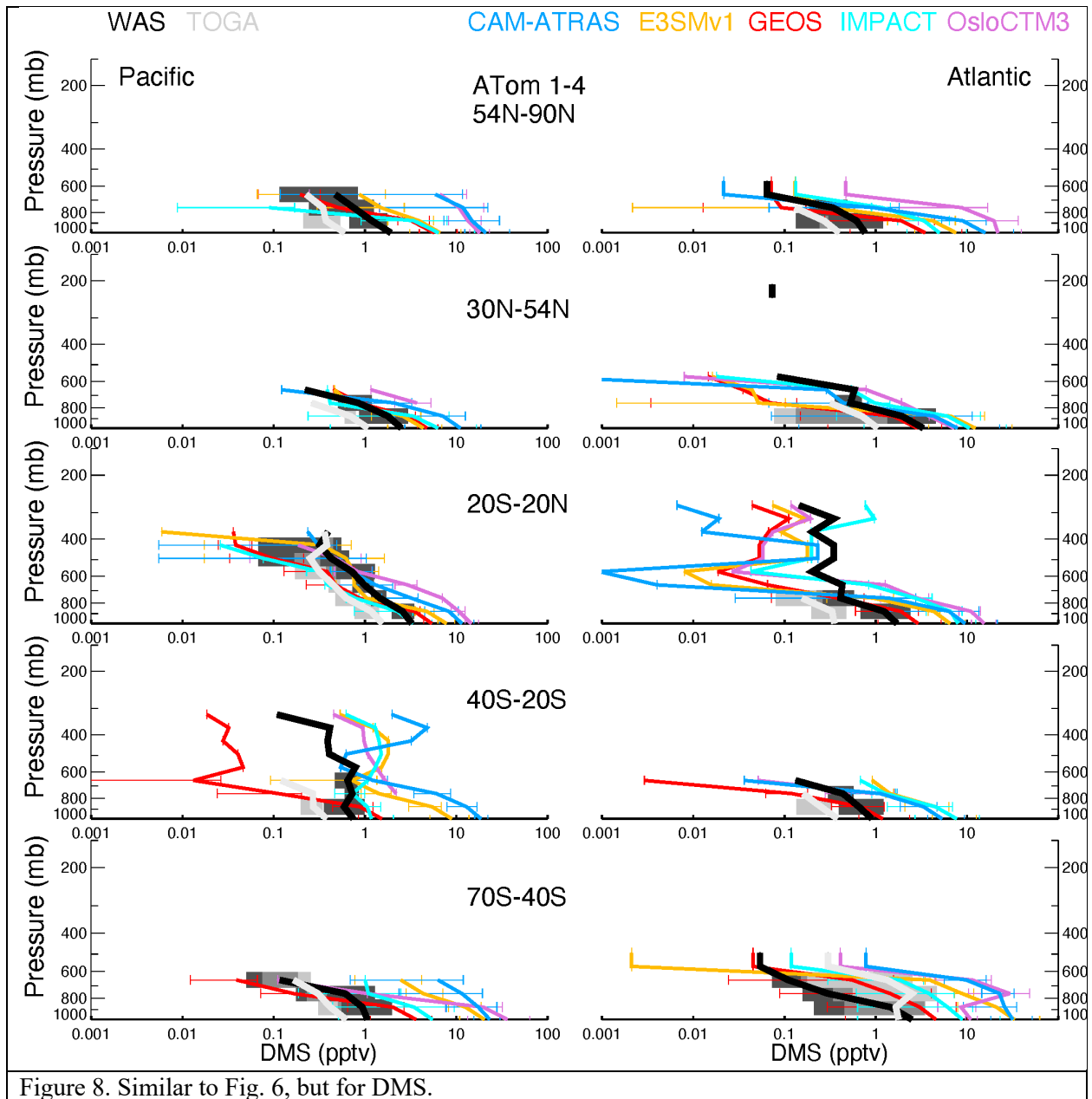
Figure 8. Similar to Fig. 6, but for DMS.

1261

1262

1263

1264

Figure 9. Similar to Fig. 6, but for MSA.
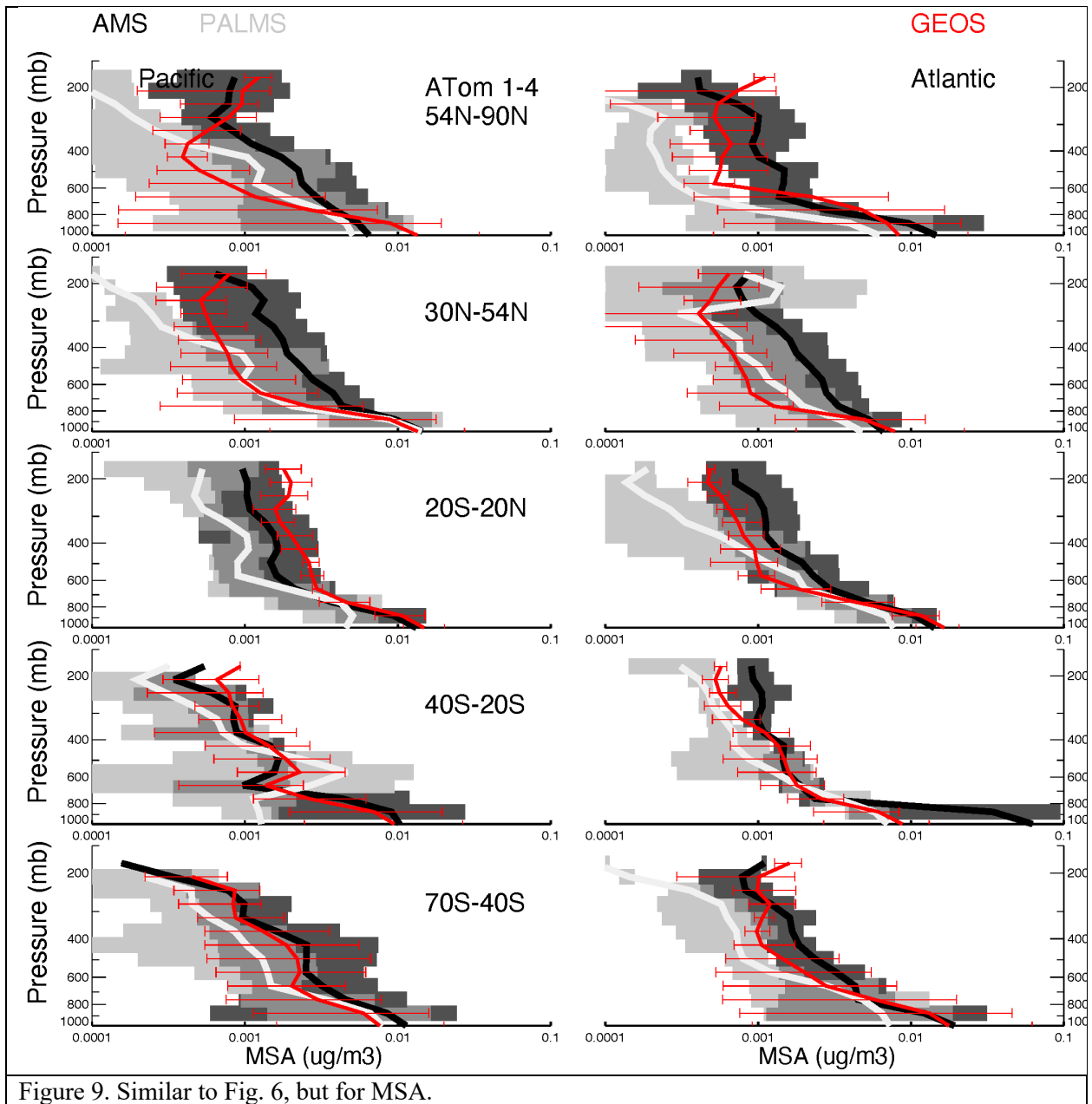
1265
1266
1267
1268
1269
1270
1271
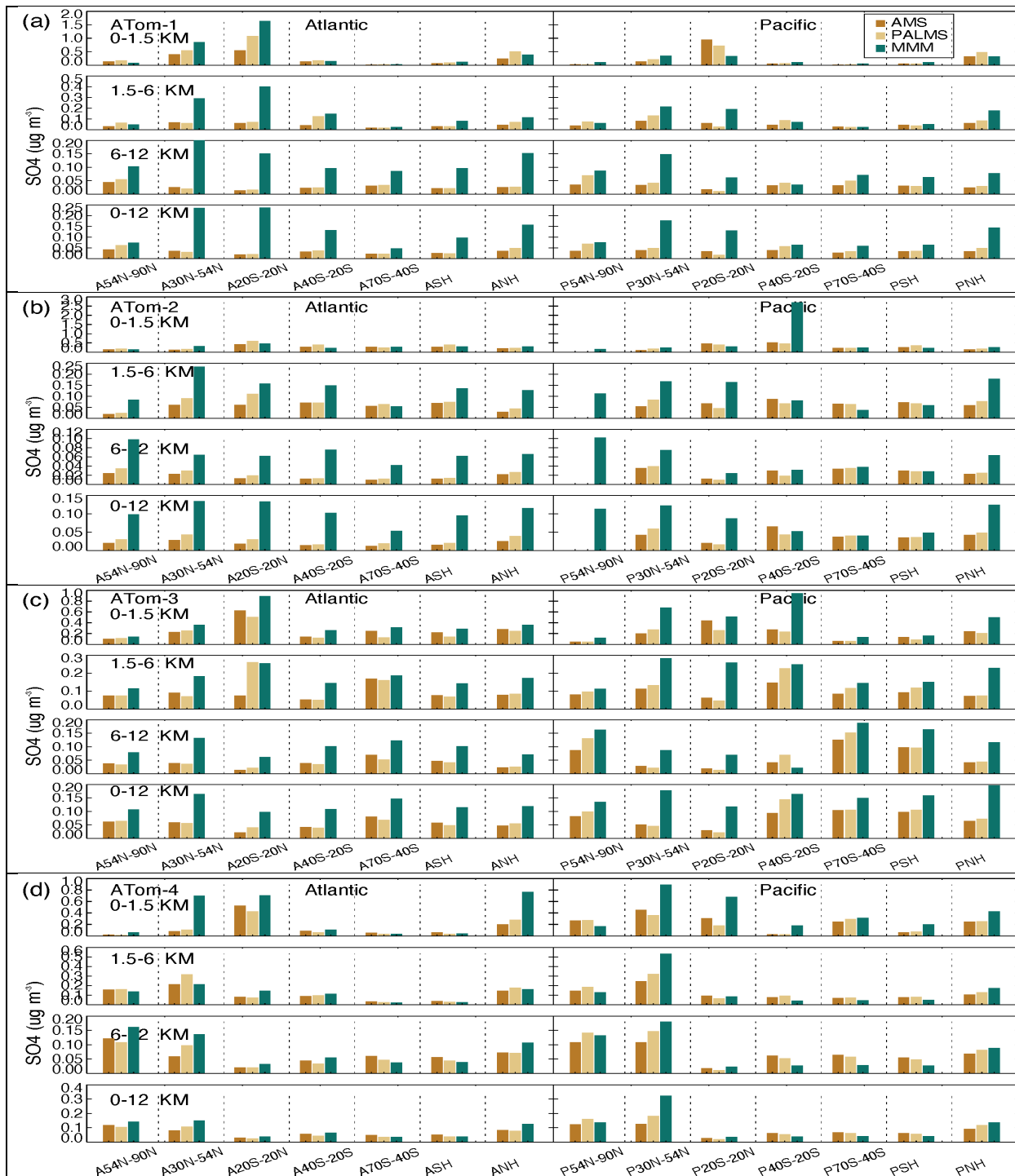
Figure 10. Median SO₄ concentrations from two measurements (AMS orange and PALMS yellow) and multi-model simulation (green) at seven latitudinal bands (including SH and NH) and four vertical layers (i.e., 0-1.5 km, 1.5-6 km, 6-12km, and 0-12 km) over Atlantic and Pacific oceans for four ATom deployments (a-d).

1272
1273
1274
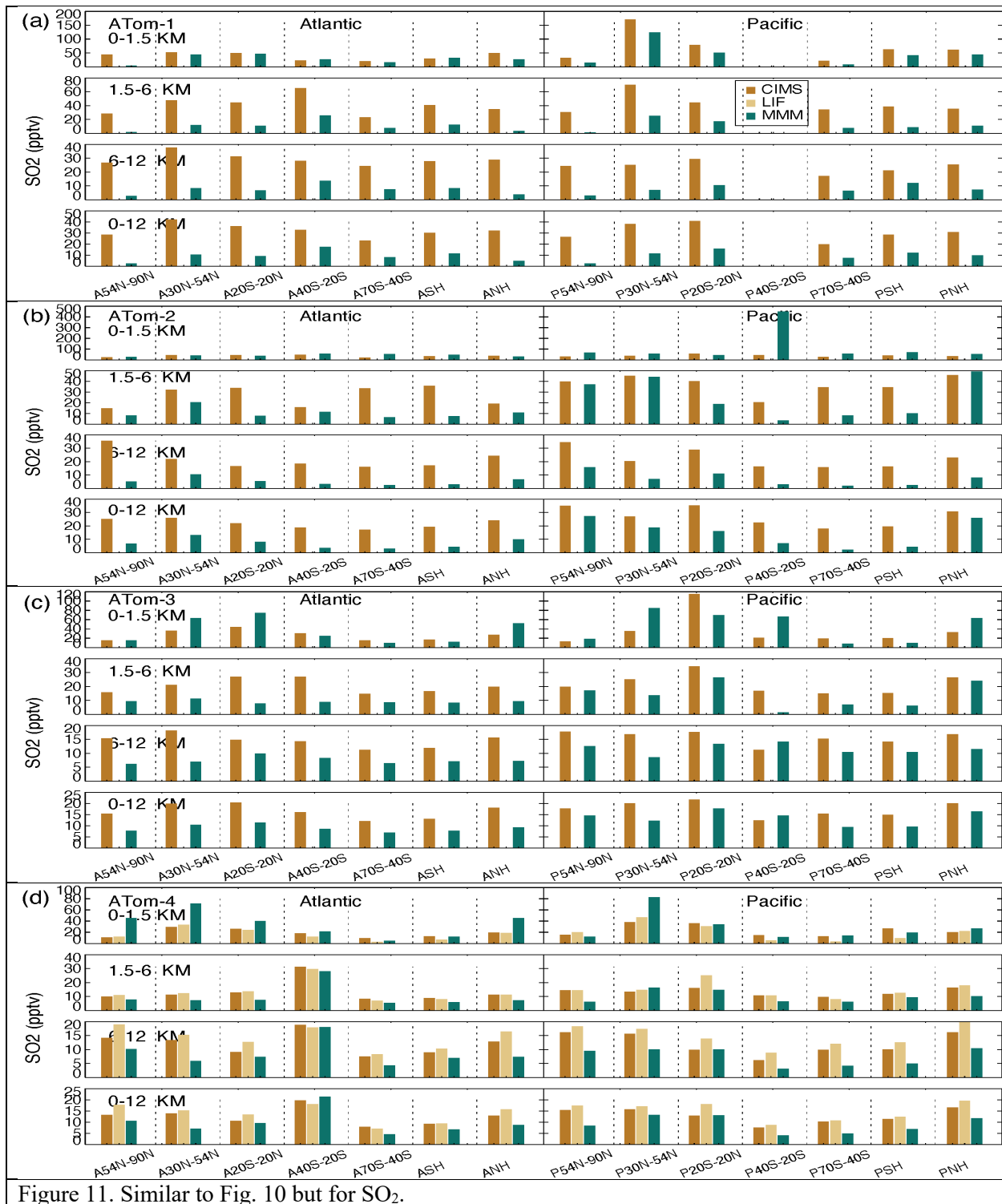
Figure 11. Similar to Fig. 10 but for SO₂.
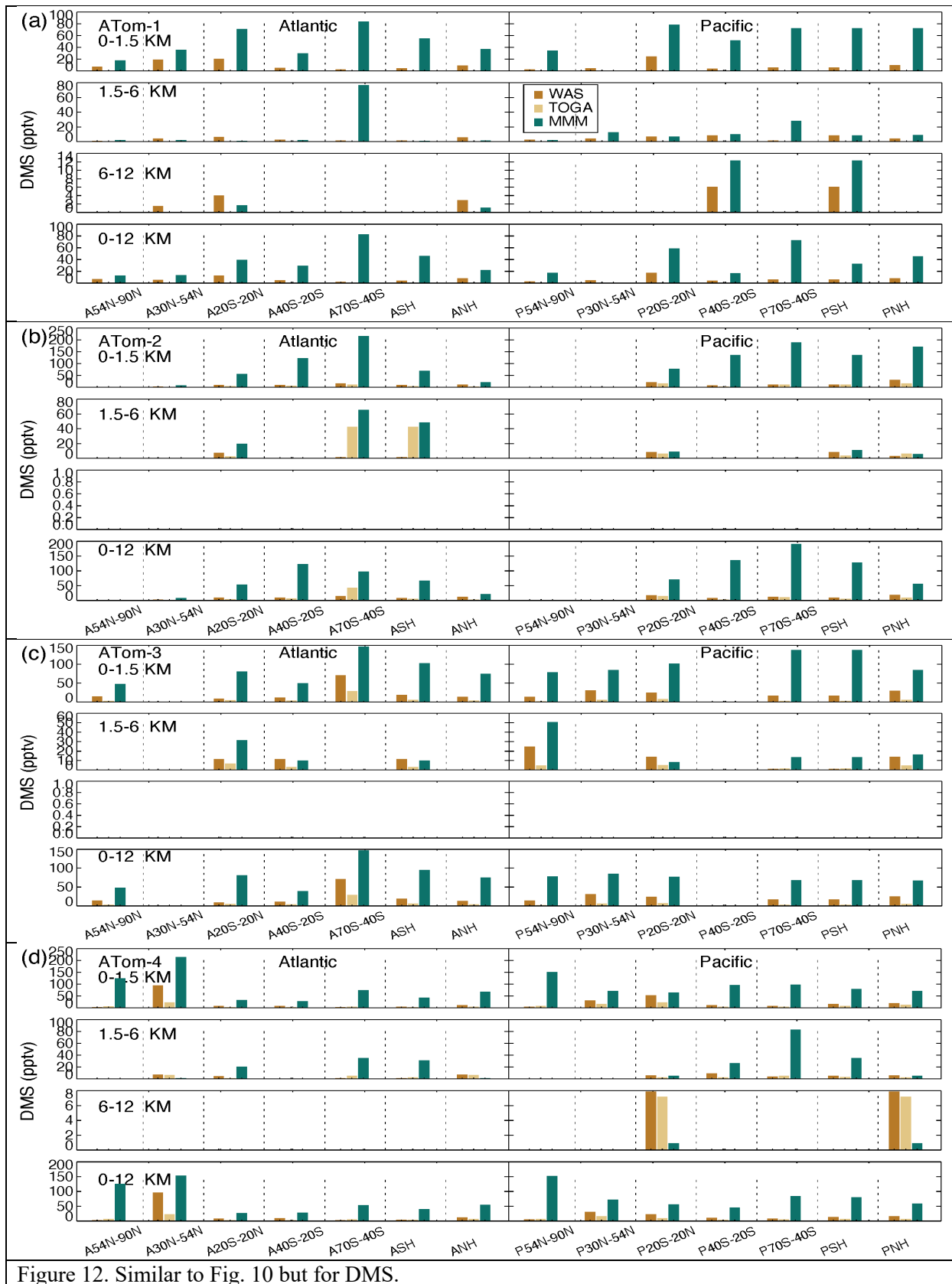
Figure 12. Similar to Fig. 10 but for DMS.

1280
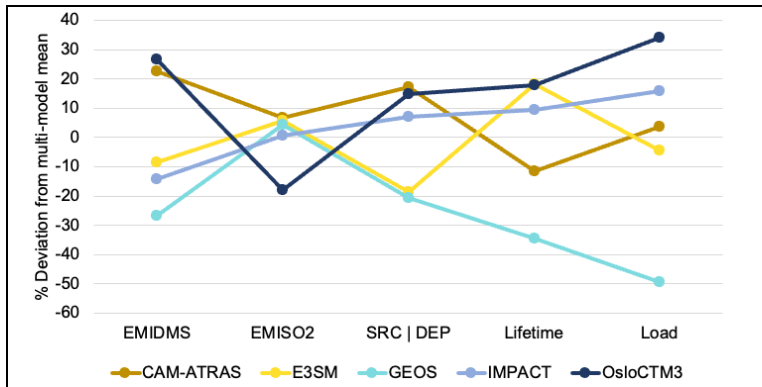
Figure 13. Deviation from multi-model mean for key budget items in sulfur study include DMS emission, SO_2 emission, sulfate source or total deposition, sulfate lifetime, and total sulfate atmospheric mass load.

1282
1283
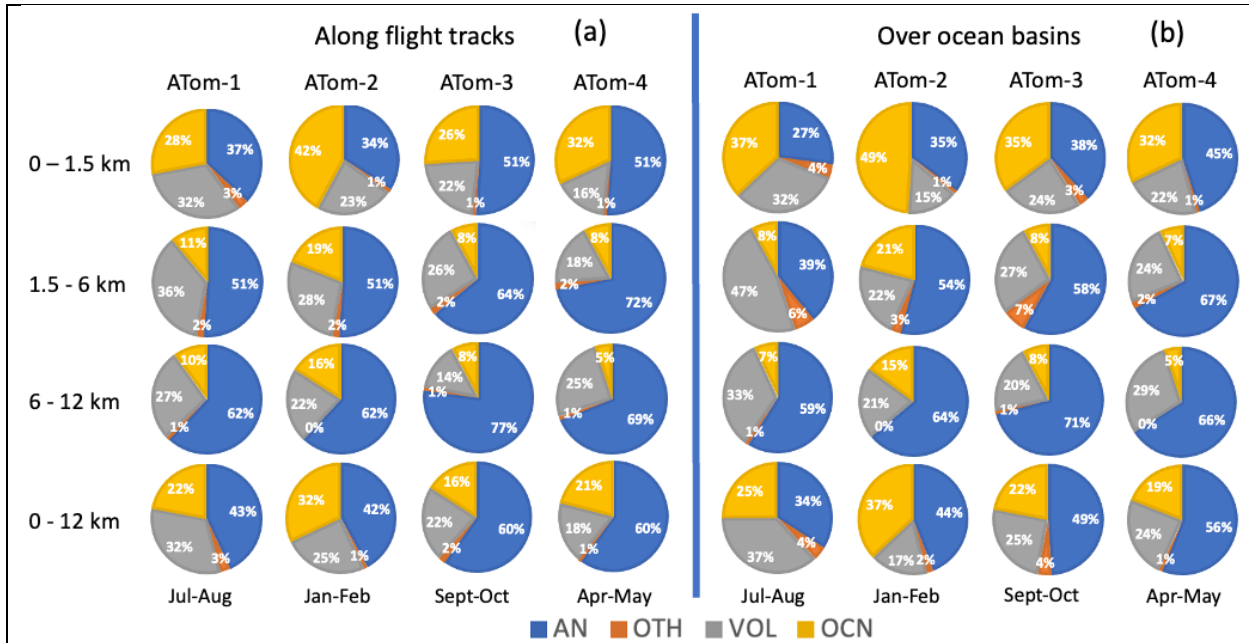
Figure 14. Source origins in percentage (%) for aerosol SO_4 along flight tracks (a) and for a wide oceanic area (b) based on the results from GEOS. Source origins are identified as anthropogenic (AN), volcanic (VOL), oceanic (OCN), and other sources (OTH). Ocean basins include shaded region shown in Fig. 1.

1284